Internal shear layers in librating spherical shells: the case of periodic characteristic paths

Jiyang He, Benjamin Favier, Michel Rieutord, Stéphane Le Dizès

Internal shear layers in librating spherical shells: the case of periodic characteristic paths

Jiyang He[1]†, Benjamin Favier[1], Michel Rieutord[2] and Stéphane Le Dizès[1]

[1]Aix Marseille Univ, CNRS, Centrale Marseille, IRPHE, Marseille, France

[2]IRAP, Université de Toulouse, CNRS, UPS, CNES, 14 avenue Édouard Belin, F-31400 Toulouse, France

(Received xx; revised xx; accepted xx)

Internal shear layers generated by the longitudinal libration of the inner core in a spherical shell rotating at a rate Ω^* are analysed asymptotically and numerically. The forcing frequency is chosen as $\sqrt{2}\Omega^*$ such that the layers issued from the inner core boundary at the critical latitude in the form of concentrated conical beams draw a simple rectangular pattern in meridional cross-sections. The asymptotic structure of the internal shear layers is described by extending the self-similar solution known for open domains to closed domains where reflections on the boundaries occur. The periodic nature of the ray path ensures that the internal shear layers remain localised around the periodic orbit. The solution obtained by summing infinitely many cycles is found to converge. The asymptotic predictions are compared to direct numerical results obtained for Ekman number as low as $E = 10^{-10}$. The agreement between the asymptotic predictions and numerical results is shown to improve as the Ekman decreases. The scalings $E^{1/12}$ for the amplitude and $E^{1/2}$ for the dissipation rate predicted by the asymptotic theory are recovered numerically. Since the self-similar solution is singular on the axis, a new local asymptotic solution is derived close to the axis and is also validated numerically. This study demonstrates that, in the limit of vanishing Ekman numbers and for particular frequencies, the main features of the flow generated by a librating inner core are obtained by propagating through the spherical shell the self-similar solution generated by the singularity at the critical latitude on the inner core.

1. Introduction

In astrophysical fluid bodies, such as metallic liquid cores and subsurface oceans, complex fluid flows can be excited by mechanical forcing (Le Bars et al. 2015). Libration, precession and tides, which correspond to harmonic perturbations of the rotation rate, rotation axis and body shape respectively, are the most common large-scale forcing originating from gravitational interactions between orbiting bodies. Libration in particular is crucial for quasi-synchronised bodies locked in a spin-orbit resonance with their orbiting companion. The amplitude of the response to libration forcing helps constrain the internal structure of astrophysical bodies, indicating, for example, the existence of a subsurface ocean in Enceladus (Thomas et al. 2016). The internal flows driven by such forcing have been extensively studied both numerically (Calkins et al. 2010; Cébron et al.

† Email address for correspondence: he@irphe.univ-mrs.fr

2012; Favier et al. 2015) and experimentally (Noir et al. 2009, 2012; Grannan et al. 2014; Le Reun et al. 2019).

In a rotating fluid, the Coriolis acceleration acts as a restoring force leading to the propagation of inertial waves whose frequency ω^* is smaller than twice the rotation rate Ω^* (Greenspan 1968). In closed geometries, propagating inertial waves can eventually form global modes which can be resonantly excited by an external forcing (Aldridge & Toomre 1969). While analytical inviscid solutions exist for simple geometries such as the cylinder or the sphere, the ill-posedness of the inviscid problem in a closed domain implies that singularities are the norm rather than the exception. Even when inviscid modes exist, such as for the cylinder, viscous corrections at the corners tend to spawn internal shear layers (McEwan 1970). In a spherical shell, two types of inviscid singularities are observed. Attractors are formed by the gradual convergence of characteristics along which inertial wave beams propagate (Rieutord et al. 2001; Rieutord & Valdettaro 2018). A second type of singularity appears wherever the boundary is locally tangent to the direction of propagation of inertial waves, the so-called critical latitude (Kerswell 1995). Viscosity is naturally regularising these inviscid attractors and the singular surfaces associated with critical latitudes, which gives rise to different types of internal shear layers propagating in the bulk of the rotating fluid. These shear layers are also relevant to stratified fluids, which can support internal gravity waves that are very similar at the linear level with inertial waves in rotating fluids. Internal and inertial attractors have been experimentally found in a rectangular basin with one sloping boundary by Maas et al. (1997) and Manders & Maas (2003) respectively. The internal shear layers spawned by critical latitudes on concave and convex boundaries have also been observed experimentally in a precessing spheroid (Noir et al. 2001) and librating (spherical and ellipsoidal) shells (Koch et al. 2013; Lemasquerier et al. 2017), respectively. They could play an important role in the mixing of stratified fluids (Brouzet et al. 2016; Dauxois et al. 2018) and the generation of zonal flows in rapidly-rotating fluid bodies (Maas 2001; Morize et al. 2010; Favier et al. 2014; Le Dizès 2015).

The dependence of oscillating internal shear layers on frequency has been tackled both as eigenvalue (Rieutord & Valdettaro 1997; Rieutord et al. 2001, 2002; Rieutord & Valdettaro 2018) and forced problems (Ogilvie 2009; Rieutord & Valdettaro 2010; Lin & Ogilvie 2018, 2021). Eigenmodes computed with the first approach are categorised as attractors, critical-latitude and quasi-regular modes based on the path of characteristics (Rieutord & Valdettaro 2018). For the forced problem, the response is classified as resonant, non-resonant or anti-resonant when its dissipation increases, remains constant or vanishes as viscosity tends to zero (Rieutord & Valdettaro 2010). The anti-resonant response occurs at the frequencies of periodic orbits. The non-resonant counterpart is observed at the frequencies of attractor modes, while the resonant one corresponds to the frequencies where global modes are hidden beneath the localised wave beams (Lin & Ogilvie 2021).

There are numerous theoretical and numerical studies investigating the scaling laws of oscillating internal shear layers. It is now accepted that the width of the shear layers spawned from the critical latitude scales like $E^{1/3}$ (Walton 1975b; Kerswell 1995), where E is the Ekman number measuring the importance of viscosity compared to rotational effects. Such a scaling has been demonstrated in several numerical works (Favier et al. 2014; Lin & Noir 2020). However, the scaling for the amplitude of the response is disputed in the literature. Early theoretical predictions by Kerswell (1995) asserted that the strength of the internal shear layers spawned from the inner boundary in a spherical shell should follow a $E^{1/6}$ scaling, which is also observed numerically (Calkins et al. 2010; Favier et al. 2014; Cébron et al. 2019). However, by asymptotically matching the

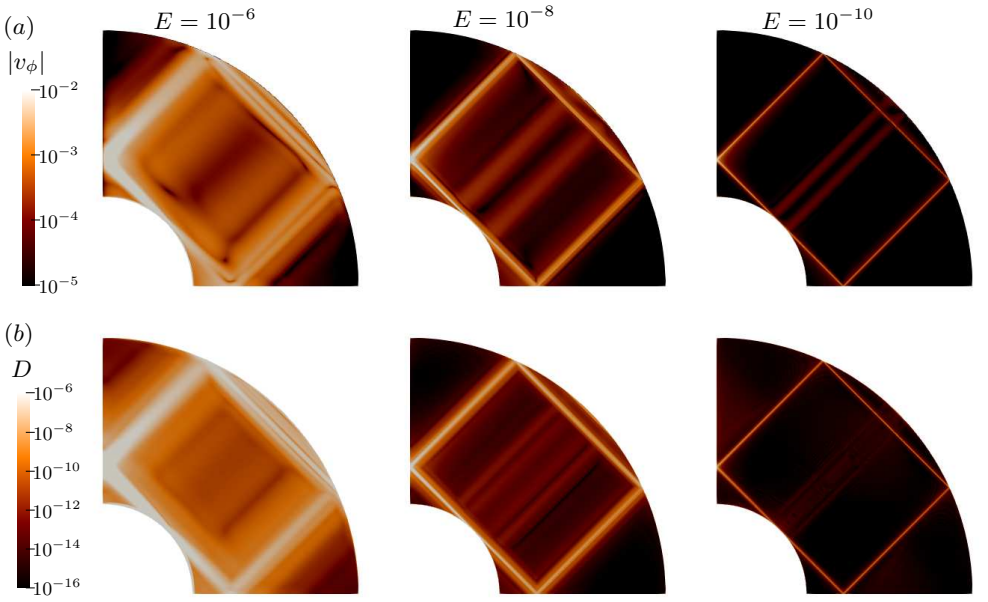

FIGURE 1. Contours of the amplitude of azimuthal velocity $|v_\phi|$ (a) and dissipation D (b) for three Ekman numbers obtained by the direct numerical integration of the linear forced viscous problem. The aspect ratio of the spherical shell is $\eta = 0.35$ and the dimensionless librating frequency of the inner core is $\omega = \sqrt{2}$.

solution of the internal shear layer to that of the boundary layer near the critical latitude, Le Dizès & Le Bars (2017) found that the amplitude should scale with $E^{1/12}$. Recent numerical results by Lin & Noir (2020) at Ekman number in the range $10^{-7} < E < 10^{-5}$, namely at lower viscosities than previous work, tend to favour the scaling $E^{1/12}$ over $E^{1/6}$. In the present paper, we will further validate the amplitude scaling $E^{1/12}$ by reaching Ekman numbers as low as $E = 10^{-10}$.

One of the difficulties associated with these internal shear layers is their behaviour as they bounce on solid boundaries. Moore & Saffman (1969) and Thomas & Stevenson (1972) introduced self-similar solutions to describe the wave beams in unbounded geometries for rotating and stratified fluids respectively. These similarity solutions are leading order expressions describing the viscous smoothing in a $O(E^{1/3})$ layer of a local inviscid singularity propagating along a characteristic line. Le Dizès & Le Bars (2017) applied these solutions to the case of the critical latitude singularity on a librating axisymmetric convex surface. They also numerically demonstrated the ability of the self-similar solutions to describe the internal shear layers generated by librating spheroid in an unbounded domain. In a bounded domain, such as a spherical shell, where reflections on the boundaries and attractor singularities exist, the similarity solutions were found to be able to describe the internal shear layers created by the critical latitude singularity (Walton 1975a) and attractors (Rieutord et al. 2001; Ogilvie 2005). However, the reflections on the solid boundaries were not considered by these previous studies. While several theoretical works provide the reflection law on flat surfaces when the boundary is not aligned with the direction of propagation (Phillips 1966; Kistovich & Chashechkin 1994; Le Dizès 2020), a more general assessment of these asymptotic solutions and the way they reflect on curved boundaries in closed geometries is nevertheless required.

In this paper, we consider the inertial waves generated by the longitudinal libration of the inner core of a rotating spherical shell in the linear limit of infinitesimal forcing ampli-

tudes and Ekman numbers. The objective is to generalise the work of Le Dizès & Le Bars (2017) to the case of a closed geometry involving reflections on curved solid boundaries. For simplicity, we do not consider the case of attractors and focus on the shear layer spawned from the critical latitude at a particular frequency for which the characteristic path eventually comes back to the critical latitude after several reflections. These periodic orbits (Rieutord et al. 2001; Rieutord & Valdettaro 2018) are a natural choice since the path of characteristics remains topologically simple, which would not be the case for frequencies sustaining attractors. For illustration, the shear layers in a spherical shell forced by the libration of the inner core are displayed in figure 1. This solution is obtained by the direct numerical integration of the linearised viscous equations and will serve as a reference to which the generalised asymptotic solution introduced in this paper will be systematically compared.

The paper is organised as follows. Section 2.1 introduces the setting of the problem and the basic equations. Then we describe the asymptotic theory in section 2.2. The self-similar solution in open geometry and its scaling are recalled in section 2.2.1. In section 2.2.2, we derive the reflection law on a curved boundary. The extended asymptotic solution in a bounded domain is derived in section 2.2.3. Section 2.3 is devoted to the description of the numerical method to directly integrate the linearised equations. The comparison between the theoretical self-similar predictions and numerical results are made in section 3 for the solution in the bulk. Motivated by the singularity of the self-similar solution on the axis, the asymptotic solution around the axis is derived using Hankel transforms and a comparison with numerical solutions is also made in section 4. Finally, a summary and possible directions for future works are discussed in section 5.

2. Framework

2.1. *Basic equations*

We consider the viscous incompressible rotating flow filling a spherical shell and forced by the libration of the inner core, as shown in figure 2. The radii of the outer and inner spheres are ρ^* and $\eta\rho^*$ (with $0 < \eta < 1$), respectively. The flow between them rotates around the symmetry axis Oz and with an angular velocity Ω^* . The inner core librates at an amplitude ε^* and frequency ω^*, such that the corresponding angular rotation rate is $\Omega^* + \varepsilon^* \cos(\omega^* t^*)$. Space and time variables are non-dimensionalized by the outer radius ρ^* and angular period $1/\Omega^*$ respectively. The non-dimensional radii of the outer and inner shells are then 1 and η respectively, while the non-dimensional angular velocity of the inner core is $1 + \varepsilon \cos \omega t$ with libration amplitude $\varepsilon = \varepsilon^*/\Omega^*$ and libration frequency $\omega = \omega^*/\Omega^*$. The Ekman number is defined by

$$E = \frac{\nu}{\Omega^* \rho^{*2}} \tag{2.1}$$

with ν being the kinematic viscosity.

Since we are concerned with the harmonic linear response in the limit of small viscosity, both the libration amplitude and the Ekman number are assumed to be small. The libration frequency ω is chosen in the inertial-wave range such that it can be written as $\omega = 2 \cos \theta_c$. The angle θ_c indicates the direction of propagation of the inertial waves with respect to the equatorial plane. It also corresponds to the inclination angle that internal shear layers make with respect to this plane. In order to form a simple closed circuit, θ_c is fixed to 45°. This means that the libration frequency ω is fixed to $\sqrt{2}$. These values are unchanged throughout the paper. An example of the ray path is shown in figure 3, where the internal shear layer is initially spawning at the critical latitude S_c and returns

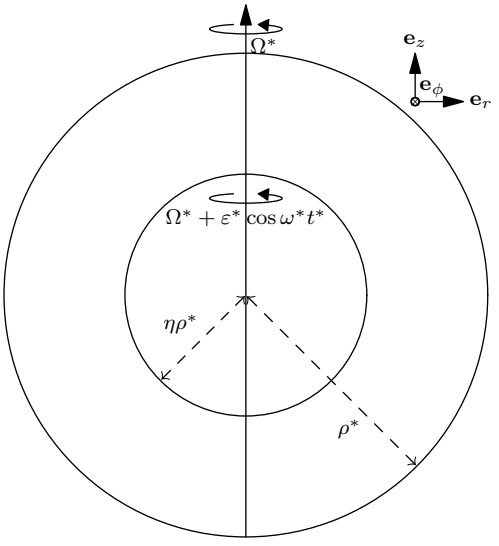

FIGURE 2. Schematic of the problem: the outer shell of radius r^* rotates with an angular velocity Ω^*, while the inner one of ηr^* rotates at $\Omega^* + \varepsilon^* \cos(\omega^* t^*)$ with ε^* and ω^* being the amplitude and frequency of the libration respectively.

to it after bouncing on the axis, reflecting twice on the outer boundary and reflecting on the equatorial plane, thanks to the imposed symmetry.

The flow is governed by the linearised incompressible Navier-Stokes equations in the rotating frame. We seek the following harmonic solution for the velocity $\boldsymbol{V}$ and pressure P

$$(\boldsymbol{V}, P) = \varepsilon(\boldsymbol{v}, p) e^{-\mathrm{i}\omega t} + c.c. \ , \tag{2.2}$$

where the notation *c.c.* denotes complex conjugate terms. The velocity $\boldsymbol{v}$ and pressure p satisfy the following equations in the rotating frame

$$-\mathrm{i}\omega \boldsymbol{v} + 2\boldsymbol{e}_z \times \boldsymbol{v} = -\nabla p + E\nabla^2 \boldsymbol{v} \ , \tag{2.3a}$$

$$\nabla \cdot \boldsymbol{v} = 0 \ , \tag{2.3b}$$

with the boundary conditions

$$\boldsymbol{v} = r\boldsymbol{e}_\phi \quad \text{on the inner shell,} \tag{2.4a}$$

$$\boldsymbol{v} = \boldsymbol{0} \quad \text{on the outer shell,} \tag{2.4b}$$

where r is the distance to the rotation axis.

2.2. *Asymptotic theory*

The asymptotic analysis is conducted within the cylindrical coordinate system (r, z, ϕ). The basic idea of the asymptotic theory is to assume that the main features of the solution come from the propagation of the critical latitude singularity S_c localised at $r = \eta\sqrt{1-\omega^2/4}$ and $z = \eta\omega/2$ on the inner sphere. For the frequency $\omega = \sqrt{2}$, this singularity is expected to propagate along the critical characteristic lines L_j $(j = 1 \dots 8)$ and form a closed circuit (see figure 3). The northward rays correspond to the rays initially propagating along the line L_1. They then cover the circuit $L_1 \to L_2 \to L_3 \to L_4 \to L_5$, possibly bounce on the inner core leading to the additional path $L_6 \to L_7 \to L_8$ before starting the circuit again. Similarly, the southward rays start propagating on the line L_5

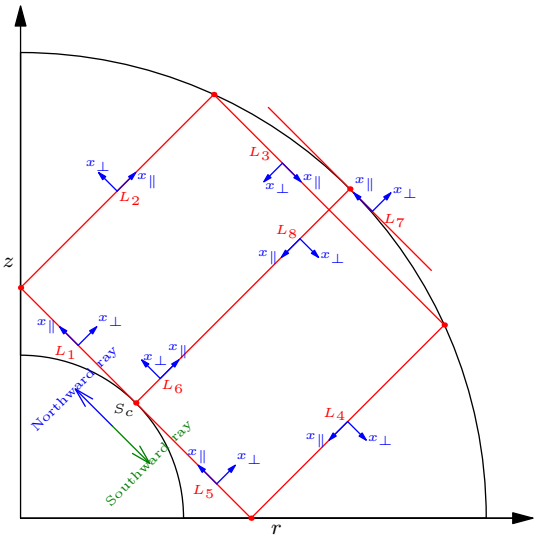

FIGURE 3. Critical lines L_j $(j = 1, 2 \dots 8)$ and the local coordinate systems $(x_\parallel, x_\perp)$ for rays initially emitted in the northward direction. The opposite directions are used for rays initially emitted in the southward direction.

from S_c, travelling on $L_5 \to L_4 \to L_3 \to L_2 \to L_1$ (possibly on $L_8 \to L_7 \to L_6$) and continuing the same circuit again. Both northward and southward rays are expected to contribute to the solution. Note however, that computing their contribution will require considering their interaction with the rotation axis and their reflections on boundaries.

For building the asymptotic solution around these critical lines, it is useful to introduce a local frame $(x_\parallel, x_\perp)$ for each critical line where $x_\perp = 0$ corresponds to the critical line itself. The variable $x_\parallel$ measures the travelled distance from the source along the critical lines. It increases as the ray propagates on each critical line. However, as we shall see below, it may exhibit a jump when the ray is reflected. The variable $x_\perp$ indicates the position with respect to the critical line. The orientation of $x_\perp$ can a priori be arbitrarily chosen. For convenience, we have assumed that the orientation does not change sign during the propagation, that is a ray at a positive $x_\perp$ stays at a positive $x_\perp$ after reflection. The orientation of the local frames shown in figure 3 is for the northward rays. Opposite local frames are taken for the southward rays.

2.2.1. *Self-similar solution and scaling*

As first shown by Moore & Saffman (1969), the propagation and viscous smoothing of a localized singularity can be described in the limit of small Ekman numbers by a self-similar solution. This result has been used and applied to the critical latitude singularity generated by the libration of a sphere in Le Dizès & Le Bars (2017). We now briefly recall the main results.

The self-similar form is derived by considering the small Ekman limit of the governing equations projected onto the local frame $(x_\parallel, x_\perp)$. The solution is characterised by $v_\parallel$, $v_\perp$, v_ϕ and p. The former two are velocity components along and perpendicular to the critical lines, while the latter two correspond to the azimuthal velocity and pressure, respectively. As the width of the internal shear layer regularised by viscosity scales with $E^{1/3}$, all quantities are expanded with the perturbation parameter $E^{1/3}$. The dependence on the radial coordinate r is removed by dividing the solution by $\sqrt{r}$. At leading order, only $v_\parallel$ and v_ϕ are required to fully describe the solution. The former has the following

self-similar form

$$v_\parallel = \frac{1}{\sqrt{r}} C_0 H_m\left(x_\parallel, \zeta\right) = \frac{1}{\sqrt{r}} C_0 \left(\frac{x_\parallel}{2\sin\theta_c}\right)^{-m/3} h_m(\zeta) \tag{2.5}$$

with the similarity variable

$$\zeta = x_\perp E^{-1/3} \left(\frac{2\sin\theta_c}{x_\parallel}\right)^{1/3} \tag{2.6}$$

and the function

$$h_m(\zeta) = \frac{e^{-\mathrm{i}m\pi/2}}{(m-1)!} \int_0^{+\infty} e^{\mathrm{i}p\zeta - p^3} p^{m-1} dp \ . \tag{2.7}$$

The real index m and the complex amplitude C_0 are the parameters characterizing the strength and the (complex) amplitude of the singularity. Expression (2.5) is a leading order expression of a viscous solution in the limit of small Ekman numbers. Next order corrections are expected to be $O(E^{1/3})$. The solution preserves the self-similar structure described by $h_m(\zeta)$ during its propagation and decay as $x_\parallel^{-m/3}$ with $x_\parallel$ being the distance from the source. Note that there are two singularities in (2.5). One is on the rotation axis where $r = 0$, the other is at the source $x_\parallel = 0$. The similarity solution is irrelevant close to these two regions. In addition, it is also irrelevant close to the boundaries where the solution should be derived following the more classical $E^{1/2}$ scaling characteristic of Ekman viscous layers.

Le Dizès & Le Bars (2017) derived the particular values of the two parameters m and C_0 for any axisymmetric convex librating object by matching the similarity solution with the boundary layer solution close to the critical latitude. As a necessary condition for matching, they obtained the particular values:

$$m = 5/4 \tag{2.8}$$

and

$$C_0 = \frac{E^{1/12}}{8(2\sin\theta_c)^{3/4}} e^{\mathrm{i}\pi/2} \quad \text{for northward ray,} \tag{2.9a}$$

$$C_0 = \frac{E^{1/12}}{8(2\sin\theta_c)^{3/4}} e^{\mathrm{i}3\pi/4} \quad \text{for southward ray.} \tag{2.9b}$$

The curvature at the critical latitude $\kappa_c = -\sin\theta_c$ for the spherical inner core has been applied. Note that there is an error about the phase of C_0 in Le Dizès & Le Bars (2017), which is corrected here. The value $m = 5/4$ implies that the ray amplitude decays as $x_\parallel^{-5/12}$. The parameters C_0 for the northward and southward rays only differ by a phase shift of $\pi/4$. These two values of C_0 only hold for the initial rays directly spawning from the source. For the subsequent reflected rays, the phase and amplitude of C_0 have to be modified as it will be in the next subsection.

The relation between the azimuthal velocity v_ϕ and the parallel velocity $v_\parallel$ is

$$v_\phi = \pm \mathrm{i} v_\parallel. \tag{2.10}$$

The sign depends on the angle between the local unit vector $\boldsymbol{e}_\parallel$ and the global unit vector $\boldsymbol{e}_r$. The + sign is taken for obtuse angles, while the − sign is taken for acute ones.

The values (2.9a,b) of C_0 clearly show that the amplitude of the leading-order asymptotic solution scales with $E^{1/12}$. Numerical results in open and closed geometries have partially confirmed such scaling at relatively high Ekman numbers (above 10^{-7})

(Le Dizès & Le Bars 2017; Lin & Noir 2020). Further evidence about this scaling at lower Ekman numbers will be provided here.

2.2.2. *Reflections on the curved boundary and on the axis*

The reflection of internal shear layers on a flat boundary has been studied by Le Dizès (2020). Here we extend this result to curved boundaries to get a better approximation of the reflected solution in a spherical shell. The idea is to take into account the finite width of the wave beam, and to consider the variation of the boundary inclination angle when the boundary is curved. This effect is illustrated in figure 4 that shows a close view of the reflection $L_2 \to L_3$ for a incident ray (in blue) located at a distance $x_\perp^i$ from the critical line indicated in red. We clearly see on this figure that the inclination angle θ^i of the boundary with respect to the incident blue ray at the reflection point R is different from the angle θ_c^i at the critical line reflection point R_c.

As in Le Dizès (2020), we still assume that the incident and the reflected ray beams preserve their self-similar structures, which are

$$v_\parallel^i = C_0^i H_m(x_\parallel^i, \zeta^i)/\sqrt{r}, \quad v_\parallel^r = C_0^r H_m(x_\parallel^r, \zeta^r)/\sqrt{r}, \tag{2.11a,b}$$

where the superscripts i and r denote the variables associated with the incident and reflected rays respectively. The relations between the incident and reflected variables are obtained by requiring the vanishing of the normal velocity at the boundary. For a ray not exactly on the critical line ($x_\perp \neq 0$; in blue in figure 4), this condition is written as $\boldsymbol{V}\cdot\boldsymbol{n} \approx -v_\parallel^i \sin\theta^i + v_\parallel^r \sin\theta^r = 0$ at the reflection point R where θ^i and θ^r are the incident and reflected angles of the rays relative to the tangent plane at the reflection point. This leads to the relation

$$\frac{C_0^i}{C_0^r} = \frac{\sin\theta^r}{\sin\theta^i}\left(\frac{x_\parallel^r}{x_\parallel^i}\right)^{-m/3} = \frac{1}{K_\theta}\left(\frac{x_\parallel^r}{x_\parallel^i}\right)^{-m/3}, \tag{2.12}$$

where K_θ denotes the ratio of the sines of the angles. The similarity variable ζ is also assumed to be preserved during reflection ($\zeta^r = \zeta^i$). This provides another relation between the ratio of the parallel coordinates and the ratio of the perpendicular coordinates

$$\frac{x_\parallel^i}{x_\parallel^r} = K_\perp^3, \tag{2.13}$$

with $K_\perp = x_\perp^i/x_\perp^r$. Thus, the ratio of amplitudes is related to K_θ and $K_\perp$ by

$$\frac{C_0^i}{C_0^r} = \frac{K_\perp^m}{K_\theta}. \tag{2.14}$$

The values of $x_\perp$ and θ can by obtained directly from figure 4. The corresponding ratios K_θ and $K_\perp$ can then be computed. Similarly to the reflection on a flat boundary (Le Dizès 2020), the reflection on a curved boundary also modifies the distance to the source and the magnitude of the incident ray. The reflected ray appears to be generated from a 'virtual' source located at the position $x_\parallel^r$ away from the reflection point R and with a strength C_0^r. Note that K_θ and $K_\perp$ are real numbers, so the phase is left unchanged by the reflection on the boundary.

We must notice that the above two expressions do not hold for rays exactly on the critical lines where $x_\perp^i = x_\perp^r = 0$ shown by the red colour in figure 4. When the rays are

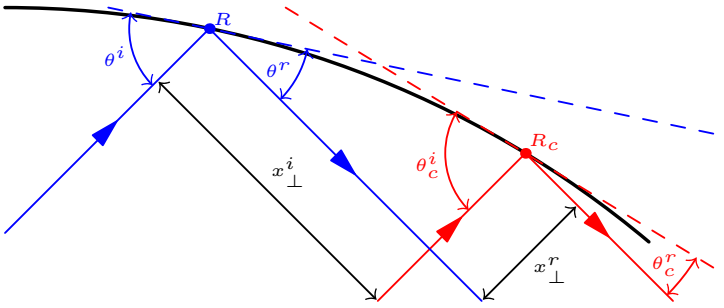

FIGURE 4. Reflection on curved boundary from the incident beam with thickness $x^i_\perp$ to the reflected beam with thickness $x^r_\perp$: red and blue lines are two rays on and off the characteristic lines; dashed lines are the tangent planes at the reflection points; θ_i and θ_r are the incident and reflected angles.

very close to the characteristic lines, the local coordinates can be expanded as

$$x^i_\parallel \approx \cos\theta^i_c s + x^i_{\parallel c}, \quad x^i_\perp \approx -\sin\theta^i_c s, \tag{2.15a}$$

$$x^r_\parallel \approx \cos\theta^r_c s + x^r_{\parallel c}, \quad x^r_\perp \approx -\sin\theta^r_c s \tag{2.15b}$$

where s is the arc length between the incidence point R and the critical reflection point R_c. Moreover, $K_\perp = K_\theta = K = \sin\theta^i_c / \sin\theta^r_c$. Now the ratios of $x_\parallel$ and C_0 take the forms

$$\frac{x^i_\parallel}{x^r_\parallel} = K^3, \quad \frac{C^i_0}{C^r_0} = K^{m-1}, \tag{2.16}$$

which are exactly the reflection law on a flat boundary (Le Dizès 2020). It is worth mentioning that viscous corrections are also present during the reflection process. These corrections are not considered in the present work. Le Dizès (2020) has shown that they are $O(E^{1/6})$ smaller and also possess a self-similar structure.

The reflection on the axis from L_1 to L_2 (see figure 3) has been discussed by Le Dizès & Le Bars (2017) and Rieutord & Valdettaro (2018), which reveals that the phase of the parallel velocity is shifted by $\pi/2$ while the amplitude and the distance to the source is kept the same. By the same method, the reverse reflection from L_2 to L_1 also shifts the phase of the parallel velocity by $\pi/2$ while keeping all other quantities unchanged. In other words, we always have on the axis:

$$C^r_0 = e^{\mathrm{i}\pi/2} C^i_0. \tag{2.17}$$

2.2.3. *Asymptotic solution in a bounded domain*

The complete asymptotic solution in a bounded domain is composed of the self-similar solutions associated with each part of rays obtained between two reflection events. Thus, it is necessary to know how rays propagate in the closed domain. For the chosen frequency $\omega = \sqrt{2}$, the ray pattern remains particularly simple. It only depends on the spherical shell aspect ratio η. In figure 5, we show the ray circuits formed by the propagation of rays for two geometries with $\eta = 0.35$ and $\eta = \sqrt{2}/2$ respectively. The former is inspired by the aspect ratio of the Earth's core while the latter is a particular case for which the critical latitude is directly connected to the pole and to the equator by a characteristic line.

The ray circuit also depends on the position of the source point relative to the critical latitude. In figure 5, we consider the ray circuits generated above (S_a; in deep blue colour)

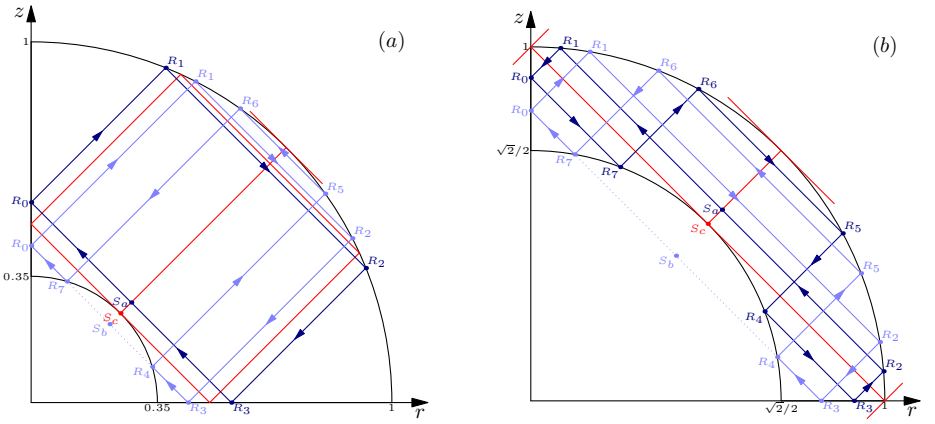

FIGURE 5. Circuits of rays in spherical shells for different radii of the inner shell: (*a*) $\eta = 0.35$; (*b*) $\eta = \sqrt{2}/2$. Red lines are characteristic lines; blue and green lines are two types of ray circuits. S_c, S_a and S_b are source points on, above and below the critical latitude respectively; $R_j (j = 0-7)$ are reflection points. The arrows on the ray circuits shows the propagation directions of the northward beam, which are opposite of those of the southward beam.

and below (S_b; in light blue colour) the critical latitude (S_c; in red colour). Each circuit is made of several directed segments. These segments are denoted as D_{ij} where i and j are start and end points respectively. These points are the reflection points on the axis and the boundaries. Specifically, R_0 is the reflection point on the axis; R_1, R_2, R_5 and R_6 are those on the outer boundary; R_3 is the one on the equator; R_4 and R_7 are those on the inner core. For the ray generated from the source below the critical latitude (S_b), the circuit consists of eight directed segments, and is the same for both geometries. As shown by the arrows on the circuits in figure 5, the sequences of directed segments that the ray propagation follows are

$$D_{70} \to D_{01} \to D_{12} \to D_{23} \to D_{34} \to D_{45} \to D_{56} \to D_{67} \quad \text{for northward rays,} \tag{2.18a}$$

$$D_{43} \to D_{32} \to D_{21} \to D_{10} \to D_{07} \to D_{76} \to D_{65} \to D_{54} \quad \text{for southward rays.} \tag{2.18b}$$

By contrast, for the ray generated from the source above the critical latitude (S_a), the circuit is different for the two values of η. There are five and nine directed segments for $\eta = 0.35$ and $\sqrt{2}/2$ respectively. The sequences of directed segments are

$$D_{S_a 0} \to D_{01} \to D_{12} \to D_{23} \to D_{3S_a}, \quad \text{for northward rays,} \tag{2.19a}$$

$$D_{S_a 3} \to D_{32} \to D_{21} \to D_{10} \to D_{0S_a} \quad \text{for southward rays} \tag{2.19b}$$

in the geometry with $\eta = 0.35$, and

$$D_{S_a 1} \to D_{10} \to D_{07} \to D_{76} \to D_{65} \to$$
$$\to D_{54} \to D_{43} \to D_{32} \to D_{2S_a} \quad \text{for northward rays,} \tag{2.20a}$$

$$D_{S_a 2} \to D_{23} \to D_{34} \to D_{45} \to D_{56} \to$$
$$\to D_{67} \to D_{70} \to D_{01} \to D_{1S_a} \quad \text{for southward rays} \tag{2.20b}$$

in the geometry with $\eta = \sqrt{2}/2$.

The asymptotic solution on every directed segment of any circuit mentioned above is described by the self-similar formula (2.5) with the same parameter $m = 5/4$, but with different values of C_0. Note that since the two sides of the shear layer (characterised by different signs of $x_\perp$) possibly have different propagation circuits, we effectively split

the beam into two independent solutions. It will become clear when we compare the asymptotic and numerical solutions why this is necessary. After one reflection on the axis, the phase of C_0 is shifted by $\pi/2$ according to the phase relation (2.17). After one reflection on the boundary, the amplitude of C_0 is scaled by the ratio (2.14). The distance $x_\parallel$ to the source is also scaled by the ratio (2.13). At the corners of a circuit where two adjacent rays intersect, the asymptotic solution is the sum of these two rays (Ogilvie 2005).

Up to this stage, we have described how to build the asymptotic solution along one complete revolution of the periodic orbit, from the critical latitude and back. However, it is natural to assume that the self-similar solution will continue propagating along the periodic characteristic path until its amplitude eventually becomes negligible. For each cycle, the self-similar nature of the local solution should be preserved since only C_0 and $x_\parallel$ are modified by reflections on the axis and boundaries. The asymptotic solution for the n^{th} cycle can be expressed by

$$\sqrt{r}v_{\parallel n} = C_n H_m(x_{\parallel n}, \zeta_n). \tag{2.21}$$

The subscript n indicates a variable associated with the n^{th} cycle. When $n = 0$, equation (2.21) is equivalent to (2.5) for the very first cycle. The variables of the subsequent cycles are related to those of the first $n = 0$ cycle by

$$x_{\parallel n} = x_{\parallel 0} + nL, \tag{2.22}$$

$$\zeta_n = \zeta_0 \left(x_{\parallel n}/x_{\parallel 0}\right)^{1/3}, \tag{2.23}$$

$$C_n = C_0 e^{\mathrm{i}n\pi/2}, \tag{2.24}$$

where L is the travelled distance within one cycle, and $\pi/2$ is the phase shift induced by the reflection on the axis occurring once per cycle. Note that L depends on the circuit (compare the deep blue and light blue circuits in figure 5*a* for instance), and it also varies along the circuit for different directed segments, but it does not change from one cycle to another (see details in Appendix A). Note also that the norm of the amplitude of the self-similar solution does not change after each cycle ($|C_n| = |C_0|$). This is associated with the symmetric character of each cycle which guarantees that the phases of contraction and expansion experienced by the beam during one cycle exactly compensate.

The complete asymptotic solution associated with one beam is thus the sum of the solution (2.21) for every cycle. After $N + 1$ cycles, we obtain

$$\sqrt{r}v_\parallel^{(N)} = \sum_{n=0}^{N} C_n H_m(x_{\parallel n}, \zeta_n). \tag{2.25}$$

The self-similar solution decays with the travelled distance as $x_\parallel^{-5/12}$ (see equations (2.5) and (2.8)). This gives a behavior in $n^{-5/12}$ of the coefficients of the series (2.25) that does not guarantee its absolute convergence. However, because C_n is oscillating with n (see equation (2.24)), the series does converge. The number of cycles can therefore be chosen as large as wanted. Using the relations (2.22-2.24), the series of the integrals (2.25) can be transformed to an integral of a geometric series

$$\sqrt{r}v_\parallel^{(N)} = C_0 \left(\frac{x_{\parallel 0}}{2\sin\theta_c}\right)^{-m/3} \frac{e^{-\mathrm{i}m\pi/2}}{(m-1)!} \int_0^\infty e^{\mathrm{i}p\zeta_0 - p^3} p^{m-1} \sum_{n=0}^{N} \mathrm{i}^n e^{-nL/x_{\parallel 0}p^3} dp. \tag{2.26}$$

Moreover, with the closed form of the geometric series the solution can be expressed by

two parts

$$\sqrt{r}v_{\parallel}^{(N)} = C_0 G_m\left(x_{\parallel 0}, x_\perp, L\right) + \varepsilon_m^{(N)}\left(x_{\parallel 0}, x_\perp, L\right) \tag{2.27}$$

with

$$G_m\left(x_{\parallel 0}, x_\perp, L\right) = \left(\frac{x_{\parallel 0}}{2\sin\theta_c}\right)^{-m/3} g_m\left(\zeta_0, L/x_{\parallel 0}\right), \tag{2.28a}$$

$$g_m\left(\zeta_0, L/x_{\parallel 0}\right) = \frac{e^{-\mathrm{i}m\pi/2}}{(m-1)!}\int_0^\infty \frac{e^{\mathrm{i}p\zeta_0 - p^3} p^{m-1}}{1-\mathrm{i}e^{-p^3 L/x_{\parallel 0}}}dp, \tag{2.28b}$$

and

$$\varepsilon_m^{(N)} = C_0\left(\frac{x_{\parallel 0}}{2\sin\theta_c}\right)^{-m/3}\frac{e^{-\mathrm{i}m\pi/2}}{(m-1)!}\int_0^\infty e^{\mathrm{i}p\zeta_0 - p^3}p^{m-1}\frac{-\mathrm{i}^{N+1}e^{-p^3L(N+1)/x_{\parallel 0}}}{1-\mathrm{i}e^{-p^3L/x_{\parallel 0}}}dp. \tag{2.29}$$

The correction term $\varepsilon_m^{(N)}$ behaves as

$$\varepsilon_m^{(N)} \sim -C_0\left(\frac{x_{\parallel 0}}{2\sin\theta_c}\right)^{-m/3}\frac{e^{-\mathrm{i}m\pi/2}}{(m-1)!}\frac{1}{3}\left(\frac{x_{\parallel 0}}{L}\right)^{5/12}\frac{\Gamma(5/12)}{1-\mathrm{i}}\mathrm{i}^{N+1}N^{-5/12}, \tag{2.30}$$

as the number of cycles becomes large. It vanishes as the number of cycles tends to infinity. Therefore, in the limit $N \to \infty$, the asymptotic solution takes the form

$$\sqrt{r}v_{\parallel} = C_0 G_m\left(x_{\parallel}, x_\perp, L\right). \tag{2.31}$$

Only the local coordinates in the very first cycle are needed to compute the asymptotic solution. Without any ambiguity, the subscript 0 denoting the very first cycle has been dropped for the parallel coordinate and similarity variable hereafter. The above discussion holds both for northward and southward rays. The final global asymptotic solution in the closed geometry is the sum of the solutions of both rays, that is

$$\sqrt{r}v_{\parallel} = C_0^{NW} G_m\left(x_{\parallel}^{NW}, x_\perp^{NW}, L\right) + C_0^{SW} G_m\left(x_{\parallel}^{SW}, x_\perp^{SW}, L\right), \tag{2.32}$$

where the superscripts NW and SW denote northward and southward rays respectively. The travelled distance L within one cycle is the same for the two rays, because they travel along the same symmetric circuit, but is different for each circuit and every directed segment shown in figure 5. More details about the computation of the circuit length L in each case can be found in Appendix A. Equation (2.32) provides the description of the parallel velocity, while the azimuthal velocity v_ϕ can be derived from the phase relation (2.10).

2.3. *Numerical method*

In order to validate the asymptotic approach, we now consider the complete numerical resolution of the linear viscous harmonic problem described in section 2.1. The governing equations (2.3) are solved numerically in spherical coordinates (ρ, ϑ, ϕ), where ρ, ϑ and ϕ are the radial distance from the center of the sphere, polar and azimuthal angles respectively. In order to compare the numerical results with asymptotic predictions obtained within a different cylindrical coordinate system, the azimuthal velocity is adopted since this velocity component is the same in both cylindrical and spherical frames.

As in Rieutord & Valdettaro (1997), the fields are expanded onto spherical harmonics in the polar and azimuthal directions and onto Chebyshev polynomials in the radial

direction. We consider the expansion

$$\boldsymbol{v} = \sum_{l=0}^{+\infty} \sum_{m=-l}^{+l} u_m^l(\rho)\boldsymbol{R}_l^m + v_m^l(\rho)\boldsymbol{S}_l^m + w_m^l(\rho)\boldsymbol{T}_l^m, \tag{2.33}$$

with

$$\boldsymbol{R}_l^m = Y_l^m(\vartheta,\varphi)\boldsymbol{e}_\rho, \quad \boldsymbol{S}_l^m = \nabla \boldsymbol{Y}_l^m, \quad \boldsymbol{T}_l^m = \nabla \times \boldsymbol{R}_l^m, \tag{2.34a-c}$$

where gradients are taken on the unit sphere. Projecting the curl of the momentum equation (2.3*a*) on this basis yields (Rieutord 1987)

$$\left.\begin{aligned} E\Delta_l w^l + \mathrm{i}\omega w^l &= -A_l\rho^{l-1}\frac{\partial}{\partial\rho}\left(\frac{u^{l-1}}{\rho^{l-2}}\right) - A_{l+1}\rho^{-l-2}\frac{\partial}{\partial\rho}\left(\rho^{l+3}u^{l+1}\right) \ , \\ E\Delta_l\Delta_l(\rho u^l) + \mathrm{i}\omega\Delta_l(\rho u^l) &= B_l\rho^{l-1}\frac{\partial}{\partial\rho}\left(\frac{w^{l-1}}{\rho^{l-1}}\right) + B_{l+1}\rho^{-l-2}\frac{\partial}{\partial\rho}\left(\rho^{l+2}w^{l+1}\right), \end{aligned}\right\} \tag{2.35}$$

with

$$A_l = \frac{1}{l\sqrt{4l^2-1}}, \quad B_l = l^2(l^2-1)A_l, \quad \Delta_l = \frac{1}{\rho}\frac{d^2}{d\rho^2}\rho - \frac{l(l+1)}{\rho^2}. \tag{2.36a-c}$$

Axisymmetry ($m = 0$) is assumed. The unknown variables in equations (2.35) are only w^l and u^l. The third component v^l is related to u^l through the continuity equation (2.3*b*), that is

$$v^l = \frac{1}{\rho l(l+1)}\frac{d\rho^2 u^l}{d\rho}. \tag{2.37}$$

The no-slip boundary conditions on the outer core impose that

$$w^l = u^l = \frac{du^l}{d\rho} = 0, \quad \text{at} \quad \rho = 1. \tag{2.38}$$

The libration on the inner boundary imposes a forcing in the azimuthal direction. Its projection onto spherical harmonics yields the inhomogeneous boundary conditions on the inner core

$$w^l = 2\sqrt{\frac{\pi}{3}}\,\eta\,\delta_{1,l}\ , \quad u^l = \frac{du^l}{d\rho} = 0 \quad \text{at} \quad \rho = \eta\ , \tag{2.39}$$

where $\delta_{i,j}$ is the Kronecker symbol.

Equations (2.35-2.39) are then discretized on the collocation points of the Gauss-Lobatto grid, which yields a linear system

$$\mathbf{A}\boldsymbol{x} = \boldsymbol{b}\ . \tag{2.40}$$

This linear algebraic system of equations is solved using the LU decomposition. The dimensions of the matrix $\mathbf{A}$ and the vector $\boldsymbol{b}$ depend on the spatial resolution which is related to the number of spherical harmonics (l_{max}) and the number of Chebyshev polynomials (N_r). For the computations at low Ekman numbers, large numbers of spherical harmonics and Chebyshev polynomials are necessary. Typically, in order to reach $E = 10^{-10}$, we use $l_{max} = 3600$ and $N_r = 1200$ which leads to a matrix size of 4323600. In that case, the memory footprint of the LU solver is approximately of 500GB.

In order to display the wave structures and the scalings, the azimuthal velocity (v_ϕ) and viscous dissipation rate (D) are computed. The latter is defined as

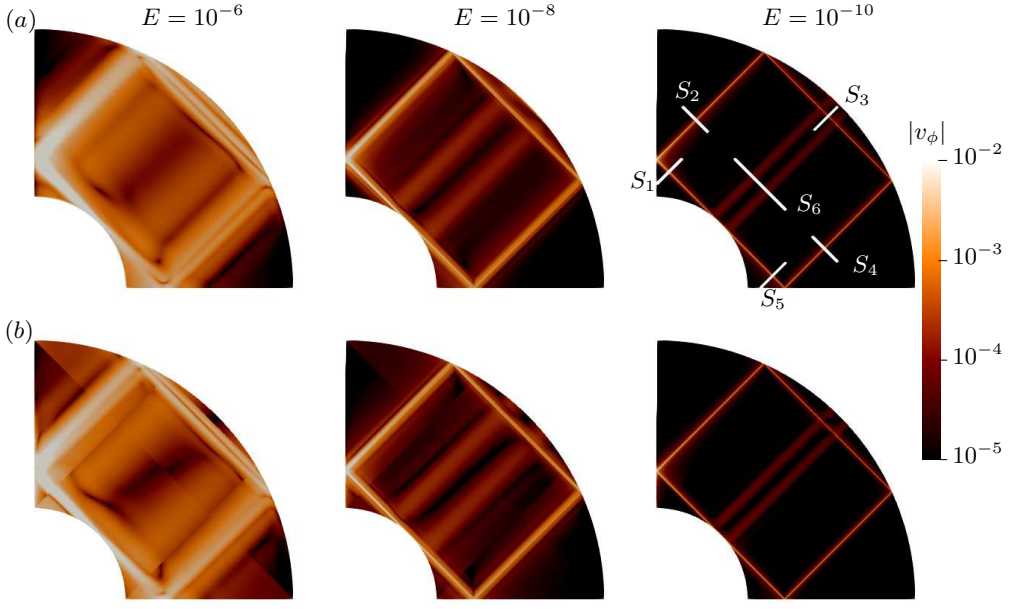

FIGURE 6. Contours of amplitudes of azimuthal velocity of numerical (a) and asymptotic (b) solutions for three Ekman numbers $E = 10^{-6}$, 10^{-8} and 10^{-10}.

(Rieutord & Valdettaro 1997)

$$D = \frac{1}{2} E \left[S_{\rho\rho}^2 + S_{\vartheta\vartheta}^2 + S_{\phi\phi}^2 + 2 \left(S_{\rho\vartheta}^2 + S_{\rho\phi}^2 + S_{\vartheta\phi}^2 \right) \right], \tag{2.41}$$

where $\mathbf{S}$ is the rate-of-strain tensor. If the amplitude of the velocity scales with $E^{1/12}$, the dissipation rate should scale with $E^{1/2}$ $(= E^{1+(1/12-1/3)\times 2})$ by the above definition. We validate this scaling numerically in the following.

3. Bulk solution

In this section, we compare the asymptotic and numerical solutions in the bulk region of the spherical shell for the two geometries $\eta = 0.35$ and $\sqrt{2}/2$ respectively. When deriving the similarity solutions (2.5-2.10), Le Dizès & Le Bars (2017) normalised lengths by the distance to the axis of the critical latitude, while lengths are non-dimensionalised by the radius of the outer shell in this paper. In order to adapt the theoretical results to our framework, the Ekman number defined by (2.1) is rescaled by $2/\eta^2$, and the coordinates rescaled by $\sqrt{2}/\eta$. The asymptotic solutions are obtained with the rescaled Ekman number and rescaled coordinates. In order to compare asymptotic and numerical solutions, the asymptotic solution has then to be divided by $\eta/\sqrt{2}$ or the numerical solutions multiplied by this quantity. The former is used when doing comparison in global coordinates, while the latter is used when doing comparison in local coordinates.

In the following, we shall only use the azimuthal component of the velocity for the comparisons. Other components of the velocity show similar behaviours, and will not be presented here.

3.1. *Aspect ratio* $\eta = 0.35$

The asymptotic solution for an infinite number of cycles is compared with the numerical one in figure 6. The inner and outer Ekman boundary layers and a region close to the

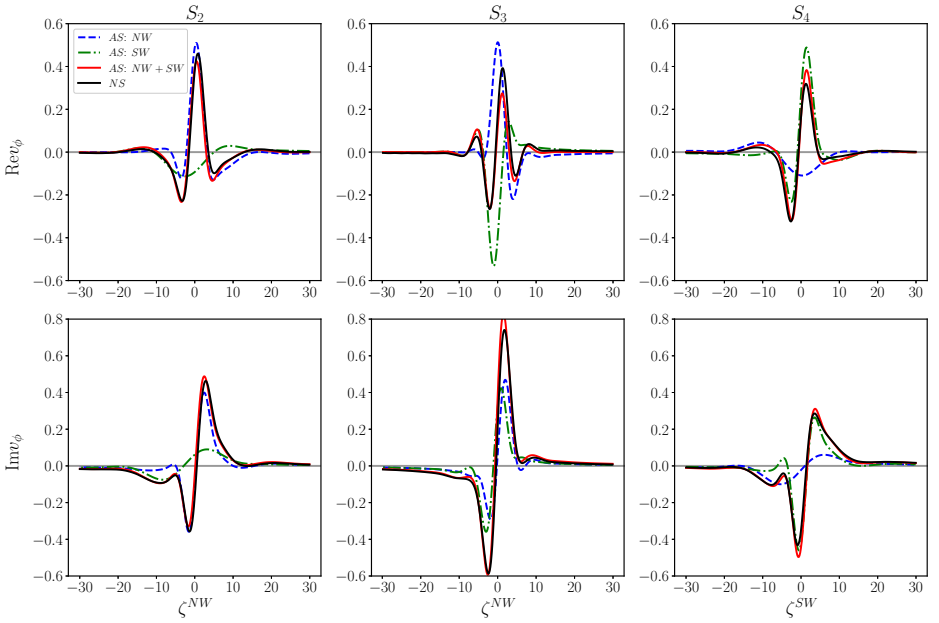

FIGURE 7. Azimuthal velocity profiles v_ϕ of the asymptotic solution (AS) for northward & southward rays and the sum of them and the numerical solution (NS) on three sections (S_2, S_3 and S_4) and at the Ekman number $E = 10^{-10}$.

axis are excluded since the asymptotic solution does not hold there. Note that we use a logarithmic colour scale over three decades in amplitude. This figure qualitatively demonstrates that our asymptotic solution can reproduce both global and local structures of the internal shear layer at the frequency $\omega^*/\Omega^* = \sqrt{2}$, especially as the Ekman number gets small. The wave structure consists of an inclined rectangle and two beams near the center line $z = r$. As the Ekman number decreases, the beams get thinner and their amplitude decreases, which is observed for both asymptotic and numerical solutions. The jumps of the asymptotic solution far away from the critical lines at high Ekman number are caused by the finite intervals of circuits' sources (see Appendix A) which tend to disappear as the Ekman number is reduced and the solution becomes more localised. In figure 6, S_{1-5} are the five sections crossing the main circuit, while S_6 is crossing the two beams near the center line $z = r$. Quantitative comparisons will be made on these sections in the following.

Figure 7 compares the asymptotic velocity profiles for the northward and southward rays independently and their sum with the numerical profiles on three sections (S_2, S_3 and S_4) and at an Ekman number of $E = 10^{-10}$. The northward ray propagates from S_2 to S_4, while the southward one propagates from S_4 to S_2. Therefore, the amplitude of the northward ray decays from S_2 to S_4, while that of the southward ray decays from S_4 to S_2. The figure shows that only the superposition of both rays can approximate the numerical solution.

The asymptotic and numerical solutions at different Ekman numbers on the section S_2 are compared in figure 8(a), which shows that our asymptotic solution performs better as the Ekman number decreases, as expected. At the lowest value of $E = 10^{-10}$, which starts to be relevant for geophysical applications, the agreement between the two solutions is

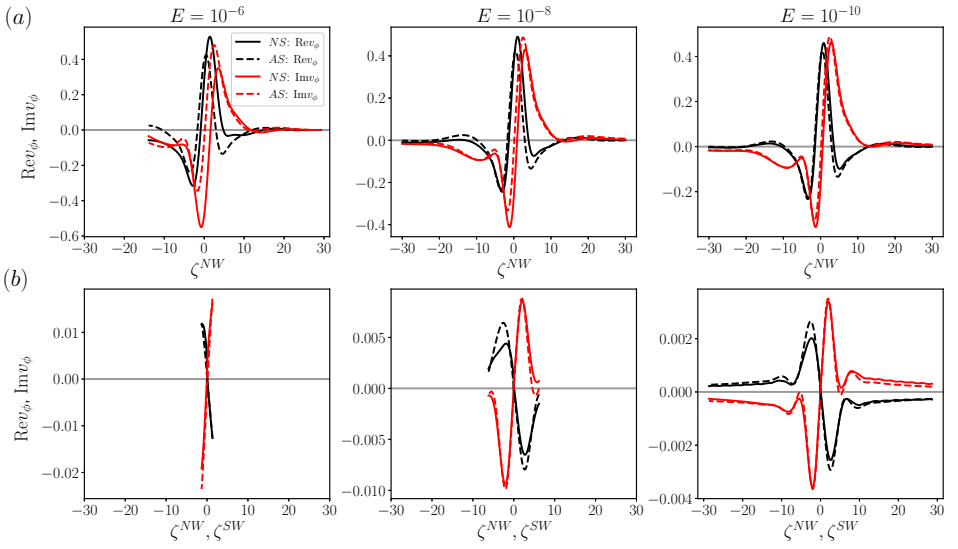

FIGURE 8. Azimuthal velocity profiles v_ϕ of the asymptotic and numerical solutions (AS and NS) at three Ekman numbers ($E = 10^{-6}$, 10^{-8} and 10^{-10}) and on the sections S_2 (a) and S_6 (b).

remarkable even far from the characteristic path. In figure 8(b), the same comparison is also made on the section S_6 where the wave beams result from the reflections of the rays generated below the critical latitude on the inner core (see the light blue circuit in figure 5(a)). Better performance of asymptotic solutions with decreased Ekman number is also observed. It demonstrates that our strategy of splitting the shear layer below and above the critical latitude is necessary and effective at reconstructing the wave beams near the center line $z = r$. Without this approach, the asymptotic solution would be vanishingly small in that region. Note that in the figure the narrower regions of the similarity variables at higher Ekman numbers are caused by the fixed length of the sections. The similarity variables on the sections take wider range of values for lower Ekman numbers (see equation (2.6)).

The physical scalings of the numerical results in the range of Ekman number $10^{-10} \leqslant E \leqslant 10^{-6}$ are presented in figure 9. A fixed point at the intersection between the critical line and the section S_2 is selected to measure both velocity amplitude and dissipation rate at various Ekman numbers. The figure shows that the velocity amplitude of the internal shear layer follows the scaling $E^{1/12}$ predicted by Le Dizès & Le Bars (2017) for an open geometry. This observation is to be contrasted with the scaling $E^{1/6}$ assumed by Kerswell (1995), who actually extrapolated the scaling of the shear layer emitted by an oscillating split disc to the one emitted a librating inner core. The foregoing numerical results show that this simple extrapolation is not valid. We note that our results also further confirm the numerical observation made by Lin & Noir (2020) at comparatively higher Ekman numbers. Regarding the dissipation rate, it follows the expected $E^{1/2}$ scaling. This scaling implies that the power dissipated in the whole shell vanishes as $E^{5/6}$ when $E \to 0$. Rieutord & Valdettaro (2010) also found such a vanishing dissipation

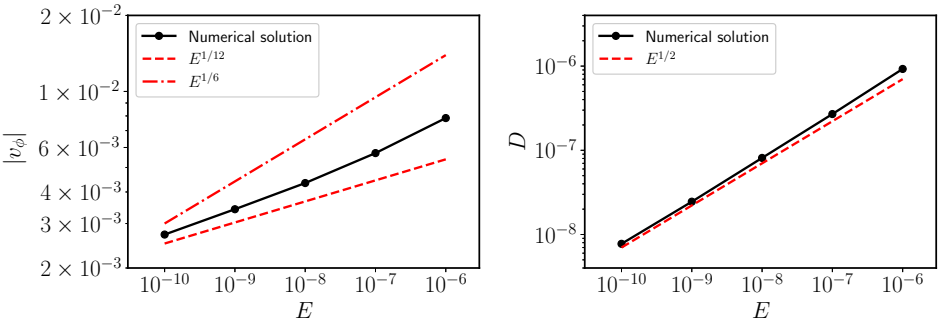

FIGURE 9. Scalings for the azimuthal velocity amplitude and dissipation rate as a function of the Ekman number. We focus on the numerical solution at the intersection between section S_2 and the critical line.

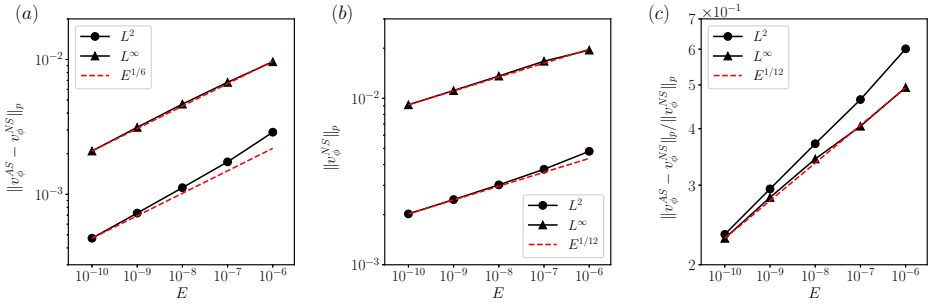

FIGURE 10. Absolute and relative errors on the azimuthal component of the velocity between the asymptotic and numerical solutions computed for the five sections S_{1-5} defined in figure 6 in the range of $-10 \leqslant \zeta \leqslant 10$ and as a function of the Ekman number.

when $E \to 0$ but with a lower power, namely as $E^{2/5}$ (see their Fig. 12). However, Rieutord & Valdettaro (2010) forced the oscillating flow with an $\mathcal{O}(1)$ body force, while in the present case the forcing vanishes as $E \to 0$. This latter point underlines the importance of the nature of the forcing in the response of the fluid and the associated viscous dissipation.

The errors of the asymptotic solution relative to the numerical one are measured on the five sections S_{1-5} in the narrow range $-10 \leqslant \zeta \leqslant 10$ around the critical lines. The solution in this narrow region is negligibly affected by the boundaries, the axis and the critical latitude where the asymptotic solution is not expected to perform well. The absolute error is measured by the norm of the difference between the theoretical predictions and numerical results averaged over the region of interest around the beam. The relative error between the two approaches is obtained by normalising with the reference numerical solution. Both L^2 and L^∞ norms are considered for Ekman numbers ranging from 10^{-6} to 10^{-10}, as shown in figure 10. For the L^2 norm, results are scaled by the square root of the number of points into the region $-10 \leqslant \zeta \leqslant 10$ since the number of points changes with the Ekman number. The absolute error plotted in figure 10(a) is shown to scale with $E^{1/6}$ for both L^2 and L^∞ norms. Figure 10(b) demonstrates that the scaling in $E^{1/12}$ of the numerical solution is very well predicted if we focus on the beam near the critical lines. This gives the relative error that is plotted in figure 10(c) with a scaling in $E^{1/12}$ as expected.

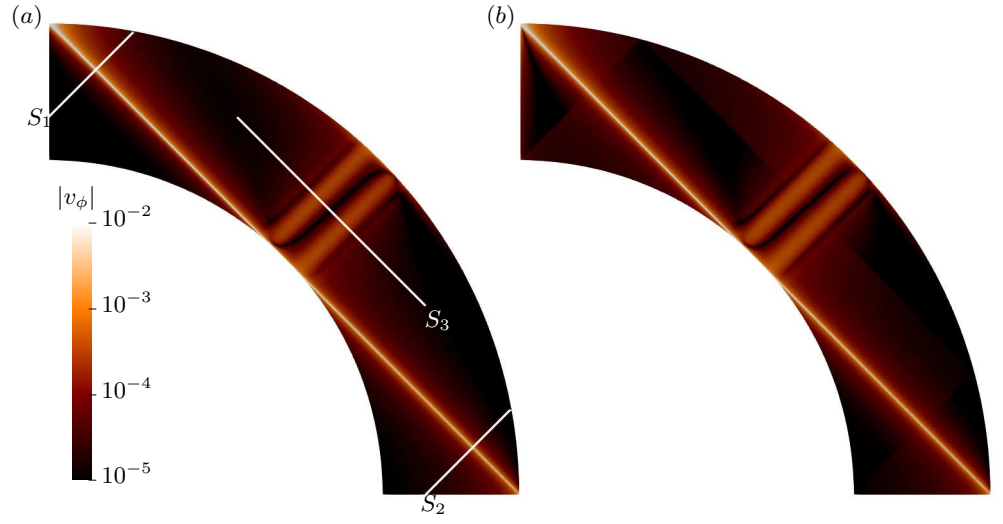

FIGURE 11. Contours of $|v_\phi|$ at $E = 10^{-10}$ and $\eta = 1/\sqrt{2}$ by numerical (a) and asymptotic (b) methods.

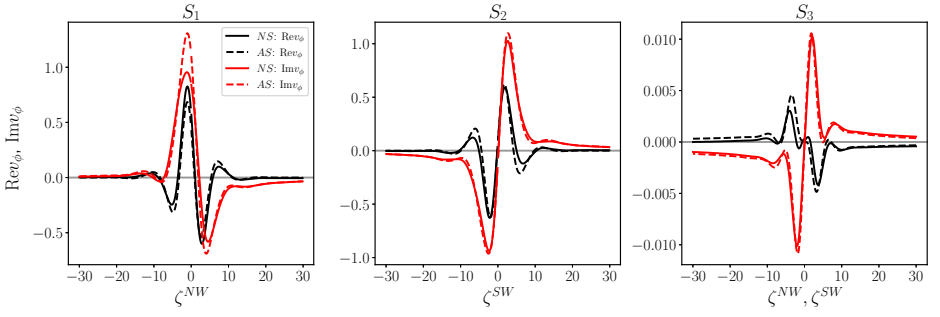

FIGURE 12. Velocity profiles along the three sections shown in figure 11 for $E = 10^{-10}$ and $\eta = 1/\sqrt{2}$.

3.2. *Aspect ratio* $\eta = 1/\sqrt{2}$

We now consider the comparison between the theoretical asymptotic predictions and numerical results in a spherical shell with an aspect ratio of $\eta = 1/\sqrt{2}$. The reason behind this choice is the peculiar nature of the critical path, which connects the critical latitude to the pole and the equator without reflection on the boundaries. We use the same asymptotic approach as described previously.

Figure 11 compares the contours of the amplitude of the azimuthal velocity at $E = 10^{-10}$. Once again, our asymptotic solution can reproduce the beam structure, including the secondary weaker beam which corresponds to secondary reflections on the inner core close to the critical latitude. The velocity profiles are compared in figure 12 for the three sections defined in figure 11. We can see that a good agreement is obtained, even for this more pathological case involving reflections near the poles. The convergence properties as the Ekman number is reduced are the same as for the previous case $\eta = 0.35$.

4. Solution close to the axis

The self-similar solution (2.32) is singular on the axis due to the term $1/\sqrt{r}$. The region close to the axis has therefore been ignored in the asymptotic results discussed so far. Around the axis, the velocity and pressure can be expressed using Hankel transform as done by Le Dizès & Le Bars (2017) in an open geometry. In this section, we generalise this approach to the case of the spherical shell where the asymptotic solution now involves a series of rays propagating in opposite directions.

4.1. *Asymptotic theory*

We consider the reflections on the axis at the intersection of two adjacent critical lines L_1 and L_2 shown in figure 3 for the aspect ratio $\eta = 0.35$. In the spherical shell, two types of rays are involved there: the northward rays that reflect from L_1 to L_2, and the southward ones that reflect from L_2 to L_1 after having performed two reflections on the outer sphere. Far away from the axis, the self-similar solution (2.32) holds. Close to the axis, the following Hankel transform for the velocity components and pressure can be used

$$v_r = \int_0^\infty U_1(k)J_1(kr)e^{\mathrm{i}\mu_1 z}dk + \int_0^\infty U_2(k)J_1(kr)e^{\mathrm{i}\mu_2 z}dk, \tag{4.1a}$$

$$v_\phi = \int_0^\infty V_1(k)J_1(kr)e^{\mathrm{i}\mu_1 z}dk + \int_0^\infty V_2(k)J_1(kr)e^{\mathrm{i}\mu_2 z}dk, \tag{4.1b}$$

$$v_z = \int_0^\infty W_1(k)J_0(kr)e^{\mathrm{i}\mu_1 z}dk + \int_0^\infty W_2(k)J_0(kr)e^{\mathrm{i}\mu_2 z}dk, \tag{4.1c}$$

$$p = \int_0^\infty P_1(k)J_0(kr)e^{\mathrm{i}\mu_1 z}dk + \int_0^\infty P_2(k)J_0(kr)e^{\mathrm{i}\mu_2 z}dk, \tag{4.1d}$$

where $J_\alpha(\alpha = 0, 1)$ are the Bessel functions of the first kind, μ_1 and μ_2 inviscid wavenumbers corresponding to the northward and southward rays respectively. The four other viscous wavenumbers that could also be present in (4.1) (see Le Dizès 2015) have been omitted here because they are not present in the internal shear layer structure and not needed to smooth the singularity on the axis as we shall see. Note also that in an open geometry, only the component μ_1 associated with the northward ray was used (Le Dizès & Le Bars 2017), since the southward ray goes to infinity and never comes back close to the axis. At leading order, the two inviscid wavenumbers are related to k by

$$\mu_1 = k\frac{\cos\theta_c}{\sin\theta_c}, \quad \mu_2 = -k\frac{\cos\theta_c}{\sin\theta_c}\ . \tag{4.2a, b}$$

The corresponding amplitudes (U_1, V_1, W_1, P_1) and (U_2, V_2, W_2, P_2) are related with each other by the following expressions (Le Dizès 2015)

$$U_{1,2} = \mathrm{i}\cos\theta_c V_{1,2}, \tag{4.3a}$$

$$W_1 = -\sin\theta_c V_1, \tag{4.3b}$$

$$W_2 = \sin\theta_c V_2, \tag{4.3c}$$

$$kP_{1,2} = -2\sin\theta_c V_{1,2}. \tag{4.3d}$$

To describe the solution close to reflection point on the axis, of coordinates $(0, \eta/\cos\theta_c)$, we introduce the local variables

$$\tilde{r} = r/E^{1/3}, \quad \tilde{z} = (z - \eta/\cos\theta_c)/E^{1/3}, \tag{4.4a, b}.$$

The Hankel transform (4.1) can then be written as

$$v_r = \mathrm{i}\cos\theta_c \left[\int_0^\infty \tilde{V}_1 J_1(\tilde{k}\tilde{r}) e^{\mathrm{i}\tilde{k}\gamma\tilde{z}} d\tilde{k} + \int_0^\infty \tilde{V}_2 J_1(\tilde{k}\tilde{r}) e^{-\mathrm{i}\tilde{k}\gamma\tilde{z}} d\tilde{k}\right], \tag{4.5a}$$

$$v_\phi = \int_0^\infty \tilde{V}_1 J_1(\tilde{k}\tilde{r}) e^{\mathrm{i}\tilde{k}\gamma\tilde{z}} d\tilde{k} + \int_0^\infty \tilde{V}_2 J_1(\tilde{k}\tilde{r}) e^{-\mathrm{i}\tilde{k}\gamma\tilde{z}} d\tilde{k}, \tag{4.5b}$$

$$v_z = \sin\theta_c \left[-\int_0^\infty \tilde{V}_1 J_0(\tilde{k}\tilde{r}) e^{\mathrm{i}\tilde{k}\gamma\tilde{z}} d\tilde{k} + \int_0^\infty \tilde{V}_2 J_0(\tilde{k}\tilde{r}) e^{-\mathrm{i}\tilde{k}\gamma\tilde{z}} d\tilde{k}\right], \tag{4.5c}$$

$$p = -2\sin\theta_c E^{\frac{1}{3}} \left[\int_0^\infty \tilde{V}_1 \frac{J_0(\tilde{k}\tilde{r})}{\tilde{k}} e^{\mathrm{i}\tilde{k}\gamma\tilde{z}} d\tilde{k} + \int_0^\infty \tilde{V}_2 \frac{J_0(\tilde{k}\tilde{r})}{\tilde{k}} e^{-\mathrm{i}\tilde{k}\gamma\tilde{z}} d\tilde{k}\right], \tag{4.5d}$$

with $\gamma = 1/\tan\theta_c$.

Expressions for $\tilde{V}_1$ and $\tilde{V}_2$ are sought by matching the solution close to the axis (4.5) with the self-similar solution in the bulk (2.32,2.10). When both $\tilde{r}$ and $\tilde{z}$ go to infinity, the limit of v_ϕ (4.5b) is

$$v_\phi \sim \frac{1}{\sqrt{2\pi\tilde{r}}} \int_0^\infty \frac{\tilde{V}_1(\tilde{k})}{\sqrt{\tilde{k}}} e^{\mathrm{i}\tilde{k}(\tilde{r}+\gamma\tilde{z})-\mathrm{i}3\pi/4} d\tilde{k} \tag{4.6a}$$

$$+ \frac{1}{\sqrt{2\pi\tilde{r}}} \int_0^\infty \frac{\tilde{V}_1(\tilde{k})}{\sqrt{\tilde{k}}} e^{\mathrm{i}\tilde{k}(-\tilde{r}+\gamma\tilde{z})+\mathrm{i}3\pi/4} d\tilde{k} \tag{4.6b}$$

$$+ \frac{1}{\sqrt{2\pi\tilde{r}}} \int_0^\infty \frac{\tilde{V}_2(\tilde{k})}{\sqrt{\tilde{k}}} e^{\mathrm{i}\tilde{k}(\tilde{r}-\gamma\tilde{z})-\mathrm{i}3\pi/4} d\tilde{k} \tag{4.6c}$$

$$+ \frac{1}{\sqrt{2\pi\tilde{r}}} \int_0^\infty \frac{\tilde{V}_2(\tilde{k})}{\sqrt{\tilde{k}}} e^{\mathrm{i}\tilde{k}(-\tilde{r}-\gamma\tilde{z})+\mathrm{i}3\pi/4} d\tilde{k} \tag{4.6d}$$

using the asymptotic behaviour of the Bessel function at infinity. The four components correspond to the incident northward rays (L_1), the reflected northward rays (L_2), the incident southward rays (L_2) and the reflected southward rays (L_1) respectively. The former two components for the incident and reflected northward rays imply that there is a phase shift from the incident to reflected rays, which is $3\pi/2$ for the azimuthal velocity. Considering the phase (2.10) between $v_\parallel$ and v_ϕ, the phase shift for $v_\parallel$ is $\pi/2$. The same is true for the southward rays.

On the other hand, the self-similar solution for v_ϕ (2.32,2.10) in the bulk takes the following form close to the intersection point on the axis ($r \to 0, z \to \eta/\cos\theta_c$)

$$v_\phi \sim \mathrm{i}\frac{1}{\sqrt{r}} C_0^{NW} G_m\left(L_{NW}, \sin\theta_c(\tilde{r}+\gamma\tilde{z}), L\right) \tag{4.7a}$$

$$+ \frac{1}{\sqrt{r}} C_0^{NW} G_m\left(L_{NW}, \sin\theta_c(-\tilde{r}+\gamma\tilde{z}), L\right) \tag{4.7b}$$

$$+ \mathrm{i}\frac{1}{\sqrt{r}} C_0^{SW} G_m\left(L_{SW}, \sin\theta_c(\tilde{r}-\gamma\tilde{z}), L\right) \tag{4.7c}$$

$$+ \frac{1}{\sqrt{r}} C_0^{SW} G_m\left(L_{SW}, \sin\theta_c(-\tilde{r}-\gamma\tilde{z}), L\right), \tag{4.7d}$$

where L_{NW} and L_{SW} are the travelled distances of the northward and southward rays from the source to the intersection point on the axis respectively. L is the travelled distance within one cycle (see Appendix A).

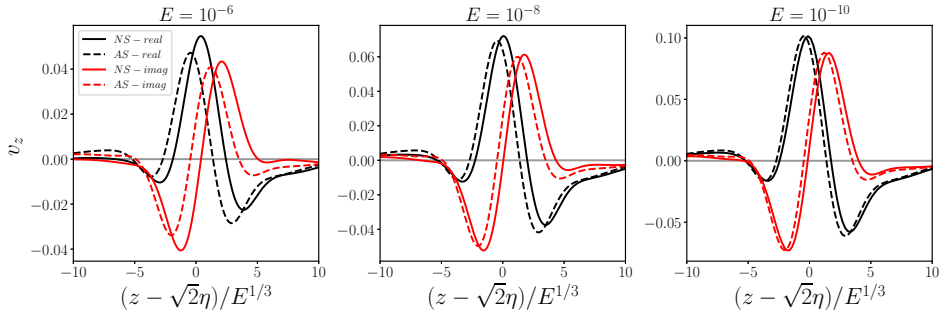

FIGURE 13. Comparison of asymptotic solutions and numerical results of v_z on the axis for three Ekman numbers.

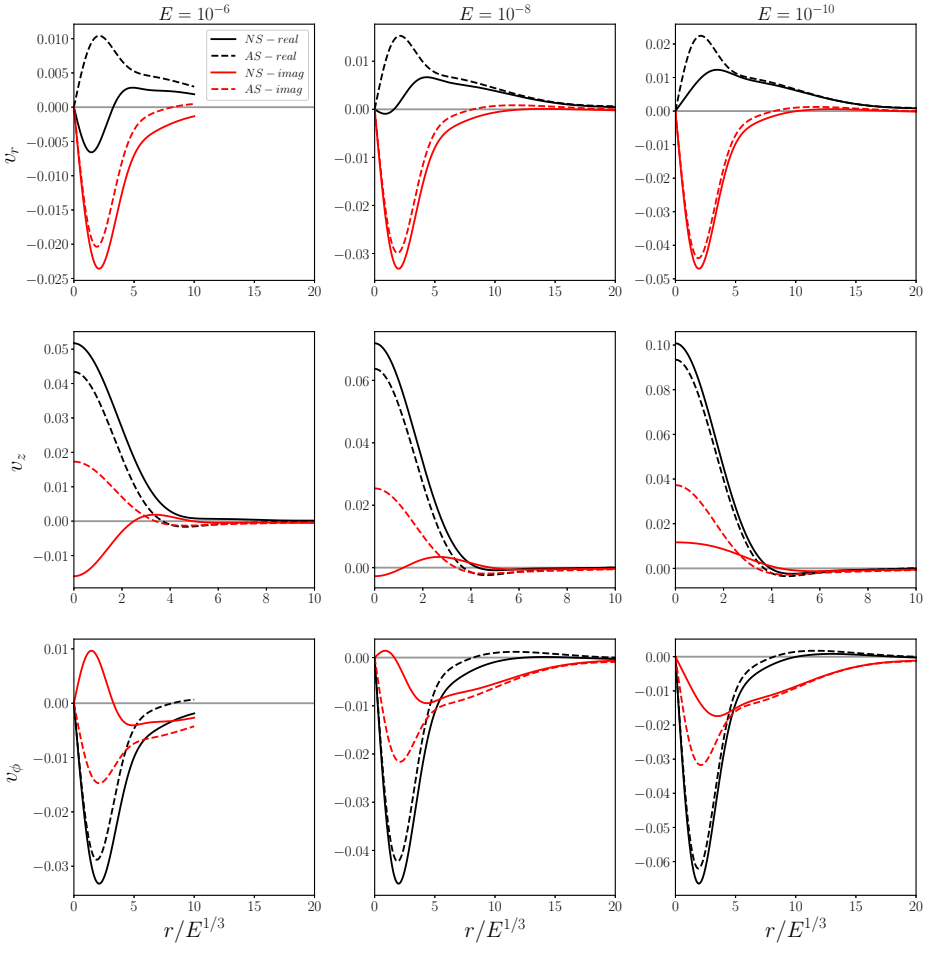

FIGURE 14. Comparison of asymptotic solutions and numerical results of three velocity components on the line perpendicular to the axis at the reflection point $(0, \eta/\cos\theta_c)$ for three Ekman numbers.

By matching (4.6) with (4.7), the amplitudes $\tilde{V}_1$ and $\tilde{V}_2$ are obtained as follows

$$\tilde{V}_1 = E^{-1/6} C_0^{NW} \sqrt{2\pi} \frac{\tilde{k}^{m-1/2}}{\sin^m \theta_c} e^{\mathrm{i}5\pi/4} \frac{e^{-\mathrm{i}m\pi/2}}{(m-1)!} \frac{e^{-L_{NW}\tilde{k}^3/(2\sin^4\theta_c)}}{1-\mathrm{i}e^{-L\tilde{k}^3/(2\sin^4\theta_c)}}, \tag{4.8a}$$

$$\tilde{V}_2 = E^{-1/6} C_0^{SW} \sqrt{2\pi} \frac{\tilde{k}^{m-1/2}}{\sin^m \theta_c} e^{\mathrm{i}5\pi/4} \frac{e^{-\mathrm{i}m\pi/2}}{(m-1)!} \frac{e^{-L_{SW}\tilde{k}^3/(2\sin^4\theta_c)}}{1-\mathrm{i}e^{-L\tilde{k}^3/(2\sin^4\theta_c)}}. \tag{4.8b}$$

It is worth pointing out the factor $E^{-1/6}$ in front of the ray amplitudes C_0^{NW} and C_0^{SW}. These amplitude are $O(E^{1/12})$, which means that $\tilde{V}_1$ and $\tilde{V}_2$ scales as $E^{-1/12}$. This implies that the solution close to the reflection point is expected to grow infinitely as E goes to zero. It clearly shows the singular nature of the small Ekman number limit for this problem: the linear solution is expected to vanish everywhere except in the boundary layer on the inner sphere (where it is finite) and at this single reflection point on the axis (where it diverges).

4.2. *Comparison with numerical results*

The asymptotic solution close to the axis (4.5) with the amplitudes (4.8) is compared with the numerical results. Figure 13 compares the asymptotic and numerical solutions along the rotation axis for three Ekman numbers. Only the velocity component v_z is concerned, as the other two components are zero by axisymmetry. We obtain a good agreement between the theoretical predictions and the numerical results. As the Ekman number decreases, our asymptotic solution converges to the numerical one. Figure 14 shows the same comparison but on the line perpendicular to the rotation axis and passing by the reflection point $(0, \eta/\cos\theta_c)$. All three velocity components are considered. Contrary to previous results, only one part of the asymptotic solution (namely the imaginary part of v_r and the real part of v_z and v_ϕ) performs well. However, as we decrease the Ekman number, the other part of the asymptotic solution approaches the corresponding numerical one, although there are still obvious differences for our lowest Ekman number 10^{-10}. Interestingly, the absolute errors of the asymptotic solution close to axis are found to be almost invariant with the Ekman number (not shown here), while the relative errors scale with $E^{1/12}$ similarly to those in the bulk (see figure 10(c)). It is suggested that both the errors of the asymptotic solutions close to axis and in the bulk come from the same source, which could be a weaker singularity at the critical latitude. It is suspected that the order of this singularity is $O(E^{1/6})$, which corresponds to $m = 1$ if its solution is still self-similar. Its contribution to the asymptotic solution is not considered here, since we are concerned with the leading-order response, but could be further investigated in future studies.

5. Conclusion

Using both numerical and asymptotic methods, we have studied the harmonic response that is generated in a rotating spherical shell by librating the inner sphere at the frequency $\omega = \sqrt{2}\Omega$ where Ω is the angular frequency of the fluid. For this particular frequency, the inertial waves propagate along rays inclined at 45 degree with respect to the equatorial plane and therefore form closed periodic orbits in a spherical shell. We have shown by considering numerical results down to Ekman numbers $E = 10^{-10}$ that the harmonic response is mainly governed by the internal shear layers that are emitted from the critical latitude of the inner sphere. In Le Dizès & Le Bars (2017), it was shown that these internal shear layers are concentrated wave beams that can be described in an open

geometry and at small Ekman numbers by the similarity solution initially introduced by Moore & Saffman (1969). Here, we have further generalised this model and constructed an asymptotic solution by monitoring the reflections of the critical latitude beams on the boundaries and on the axis. For this purpose, we have improved the known reflection rules (Le Dizès 2020) to take into account the curvature of the spherical shell boundaries. This extension has been shown to be necessary to describe the flow far from the main beam, in particular the wave beams generated by reflections on the inner core close to the critical latitude. We have finally obtained that the asymptotic solution can be written as an infinite sum of similarity solutions. Interestingly, this sum converges owing to the phase shift of $\pi/2$ that the beams experience at each reflection on the rotation axis.

The asymptotic solution has been compared to the numerical solution of the linearised equations for several Ekman numbers and two values of the shell aspect ratio, and a very good agreement has been demonstrated. The relative error has been shown to be of order $E^{1/12}$. We suspect that it could be associated with a weaker singularity at the critical latitude. An immediate consequence of our result is the scaling in $E^{1/12}$ of the harmonic response velocity, as predicted for the internal shear layer amplitude in an open geometry (Le Dizès & Le Bars 2017). This scaling was also observed in recent simulations by Lin & Noir (2020) but it contrasts with the $E^{1/6}$ scaling previously reported in the literature in similar contexts (Kerswell 1995; Calkins et al. 2010; Favier et al. 2014; Cébron et al. 2019).

We have also analysed the solution close to the point on the rotation axis where the critical latitude beam reflects. The similarity solution diverges at this point. We have provided a new asymptotic expression describing the solution in the $O(E^{1/3})$ neighbourhood of this point. We have in particular shown that the solution also scales as $E^{-1/12}$ in this region.

It is worth emphasising that the theoretical method that has been used to build the asymptotic solution can be applied to other situations. For instance, one can imagine considering other libration frequencies. As long as $\omega < 2\Omega$, critical latitude beams are expected to be excited. These beams would propagate in the spherical shell, be reflected on boundaries and form a complex ray pattern depending on the aspect ratio and the frequency. If the critical latitude beams converge towards an attractor, or if they travel along a periodic orbit, as in the present case, the solution is expected to be localised along these beams. The solution could then be obtained as a sum of similarity solutions. Because these similarity solutions decrease slowly along their direction of propagation as $x_{\parallel}^{-5/12}$, the convergence of this sum would depend on the phase shift that the beam experiences on the periodic orbit or on the attractor, that is on the number of reflection on the axis. If the sum converges, we claim that our approach should apply. The other situation where the sum does not converge is naturally of interest. We suspect that in that case one obtains a completely different response with a new scaling in E, and probably multi-layer structures as observed in the Stewartson layers between differentially rotating spheres (Stewartson 1966).

Finally, it is important to mention that we have limited our analysis to libration to be able to use an existing model for the structure of the critical latitude beam. Yet, critical latitude beams exist for other types of harmonic forcing. The Saint Andrews cross pattern (Mowbray & Rarity 1967; Greenspan 1968) obtained by translating periodically a sphere is nothing but the pattern left by the critical latitude beams. If these beams can be described by the similarity solution of Moore & Saffman (1969), a similar approach could then naturally be developed in those cases and further generalised to closed geometries.

Acknowledgements

J. He acknowledges China Scholarship Council for financial support (CSC 202008440260). Centre de Calcul Intensif d'Aix-Marseille is acknowledged for granting access to its high performance computing resources.

Declaration of interests

The authors report no conflict of interest.

Appendix A. Expressions of local coordinates and one-cycle distances

In this section, we will provide the expressions of the local coordinates $(x_\parallel, x_\perp)$ and the one-cycle distances L required by the asymptotic solution (2.32). We denote the position where the asymptotic solution is calculated as P. The ray circuit crossing P can be built by tracing the propagation of rays starting from P until a closed path is formed. The global coordinates of the circuit's vertices can be obtained from that of P. The position of the circuit's source relative to that of the critical latitude (defined as $x_{\perp S}$) can also be obtained from their global coordinates. For the circuits shown in figure 5, the positions of their sources fall into the following intervals

$$(\sqrt{2}/2-1)\eta < x_{\perp S_b} < 0, \tag{A 1a}$$

$$0 < x_{\perp S_a} < \sqrt{2}/2-\eta, \quad \text{for} \quad \eta = 0.35, \tag{A 1b}$$

$$0 < x_{\perp S_a} < \sqrt{1-\eta^2/2}-\eta, \quad \text{for} \quad \eta = 1/\sqrt{2}. \tag{A 1c}$$

These intervals are adjacent to the critical lines ($x_\perp = 0$), and the sources within them should play dominant roles over those outside them, especially when the wave beams are thinner at lower Ekman numbers. At higher Ekman numbers where wave beams are thicker, considering only the sources within these intervals creates unphysical cutoffs at the endpoints, which are illustrated in figure 6. However, these cutoffs are almost invisible at lower Ekman numbers. It should be sufficient to consider the sources within the intervals (A 1). The circuits with sources outside these intervals possess different patterns from those shown in figure 5. One can still construct the corresponding asymptotic solutions using the approach presented in this paper, in order to smooth the cutoffs at the endpoints of the intervals.

For convenience, we denote L_{ij} as the length between two points i and j. When the two points are two adjacent vertices of a circuit, L_{ij} denotes the length of the relevant directed segment. The ratio of the perpendicular coordinates between the incident and reflected rays at a reflection point i is defined as $K_{\perp i}$. $x_{\perp S}$ solely determines a circuit, and L_{ij} of the directed segments and $K_{\perp i}$ at the reflection points for the circuit can be expressed as a function of the corresponding $x_{\perp S}$.

We start with the northward rays in the geometry of $\eta = 0.35$. L_{ij} and $K_{\perp i}$ for the circuit generated by S_a (deep blue line in figure 5*a*; $x_{\perp S} > 0$) take the forms

$$L_{S_aR_0} = L_{R_3S_a} = \eta + x_{\perp S}, \tag{A 2a}$$

$$L_{R_0R_1} = L_{R_2R_3} = -(\eta + x_{\perp S}) + \sqrt{1-(\eta + x_{\perp S})^2}, \tag{A 2b}$$

$$L_{R_1R_2} = 2(\eta + x_{\perp S}), \tag{A 2c}$$

and

$$K_{\perp R_1} = 1/K_{\perp R_2} = \frac{\sqrt{1-\eta^2} + \sqrt{1-(\eta + x_{\perp S})^2}}{2\eta + x_{\perp S}}. \tag{A 3}$$

The local coordinates of P can be obtained by propagating the source S_a to the target P, during which they are scaled at the reflection points on the boundaries. On every directed segment, the local coordinates are expressed as

$$x_\parallel = L_{S_a P}, \qquad x_\perp = x_{\perp S}, \quad P \in D_{S_a R_0}, \tag{A 4a}$$

$$x_\parallel = x_{\parallel R_0} + L_{R_0 P}, \qquad x_\perp = x_{\perp S}, \quad P \in D_{R_0 R_1}, \tag{A 4b}$$

$$x_\parallel = x_{\parallel R_1}/K^3_{\perp R_1} + L_{R_1 P}, \quad x_\perp = x_{\perp S}/K_{\perp R_1}, \quad P \in D_{R_1 R_2}, \tag{A 4c}$$

$$x_\parallel = x_{\parallel R_2} K^3_{\perp R_1} + L_{R_2 P}, \qquad x_\perp = x_{\perp S}, \quad P \in D_{R_2 R_3}, \tag{A 4d}$$

$$x_\parallel = x_{\parallel R_3} + L_{R_3 P}, \qquad x_\perp = x_{\perp S}, \quad P \in D_{R_3 S_a}, \tag{A 4e}$$

where $x_{\parallel i}$ in the last four directed segments takes the parallel coordinate of P locating at the end of the previous directed segment. If we define the following formula

$$L_a = 2L_{S_a R_0} + 2L_{R_0 R_1} + L_{R_1 R_2} K^3_{\perp R_1}, \tag{A 5}$$

the one-cycle distance L for every directed segment takes the form

$$L = L_a, \quad P \in D_{S_a R_0}, D_{R_0 R_1}, D_{R_2 R_3}, D_{R_3 S_a}, \tag{A 6a}$$

$$L = L_a/K^3_{\perp R_1}, \quad P \in D_{R_1 R_2}. \tag{A 6b}$$

When P locates on the circuit generated by S_b (light blue line in figure 5*a*; $x_{\perp S} < 0$), $L_{S_b R_0}$, $L_{R_0 R_1}$, $L_{R_1 R_2}$ and $L_{R_2 R_3}$ take the same forms as those of S_a (A 2), while the rest directed segments take the lengths

$$L_{R_7 R_0} = L_{R_3 R_4} = (\eta + x_{\perp S}) - \sqrt{\eta^2 - (\eta + x_{\perp S})^2}, \tag{A 7a}$$

$$L_{R_4 R_5} = L_{R_6 R_7} = \sqrt{1 - [\eta^2 - (\eta + x_{\perp S})^2]} - (\eta + x_{\perp S}), \tag{A 7b}$$

$$L_{R_5 R_6} = 2\sqrt{\eta^2 - (\eta + x_{\perp S})^2}. \tag{A 7c}$$

$K_{\perp R_1}$ and $K_{\perp R_2}$ also take the same forms as those of S_a (A 3). The other ratios are

$$K_{\perp R_4} = 1/K_{\perp R_7} = \frac{\sqrt{-x_{\perp S}}}{\sqrt{2\eta + x_{\perp S}}}, \tag{A 8a}$$

$$K_{\perp R_5} = 1/K_{\perp R_6} = \frac{\sqrt{1 - [\eta^2 - (\eta + x_{\perp S})^2]} + 1}{\sqrt{2\eta + x_{\perp S}}\sqrt{-x_{\perp S}}}. \tag{A 8b}$$

The local coordinates of P on every directed segment are

$$x_\parallel = L_{S_b P}, \quad x_\perp = x_{\perp S}, \quad P \in D_{S_7 R_0}, \tag{A 9a}$$

$$x_\parallel = x_{\parallel R_0} + L_{R_0 P}, \quad x_\perp = x_{\perp S}, \quad P \in D_{R_0 R_1}, \tag{A 9b}$$

$$x_\parallel = x_{\parallel R_1}/K^3_{\perp R_1} + L_{R_1 P}, \quad x_\perp = x_{\perp S}/K_{\perp R_1}, \quad P \in D_{R_1 R_2}, \tag{A 9c}$$

$$x_\parallel = x_{\parallel R_2} K^3_{\perp R_1} + L_{R_2 P}, \quad x_\perp = x_{\perp S}, \quad P \in D_{R_2 R_3}, \tag{A 9d}$$

$$x_\parallel = x_{\parallel R_3} + L_{R_3 P}, \quad x_\perp = x_{\perp S}, \quad P \in D_{R_3 R_4}, \tag{A 9e}$$

$$x_\parallel = x_{\parallel R_4}/K^3_{\perp R_4} + L_{R_4 P}, \quad x_\perp = x_{\perp S}/K_{\perp R_4}, \quad P \in D_{R_4 R_5}, \tag{A 9f}$$

$$x_\parallel = x_{\parallel R_5}/K^3_{\perp R_5} + L_{R_5 P}, \quad x_\perp = x_{\perp S}/(K_{\perp R_4} K_{\perp R_5}), \quad P \in D_{R_5 R_6}, \tag{A 9g}$$

$$x_\parallel = x_{\parallel R_6} K^3_{\perp R_5} + L_{R_6 P}, \quad x_\perp = x_{\perp S}/K_{\perp R_4}, \quad P \in D_{R_6 R_7}, \tag{A 9h}$$

where $x_{\parallel i}$ in the last seven directed segments is defined as before. If we define the following formula

$$L_b = 2L_{R_7 R_0} + 2L_{R_0 R_1} + L_{R_1 R_2} K^3_{\perp R_1} + 2L_{R_4 R_5} K^3_{\perp R_4} + L_{R_5 R_6} K^3_{\perp R_4} K^3_{\perp R_5}, \tag{A 10}$$

the one-cycle distance can be expressed for every directed segment as

$$L = L_b, \quad P \in D_{R_7 R_0}, D_{R_0 R_1}, D_{R_2 R_3}, D_{R_3 R_4}, \tag{A 11a}$$

$$L = L_b/K^3_{\perp R_1}, \quad P \in D_{R_1 R_2}, \tag{A 11b}$$

$$L = L_b/K^3_{\perp R_4}, \quad P \in D_{R_4 R_5}, D_{R_6 R_7} \tag{A 11c}$$

$$L = L_b/(K^3_{\perp R_4} K^3_{\perp R_5}), \quad P \in D_{R_5 R_6}. \tag{A 11d}$$

It is worth mentioning that although L and $x_\parallel$ exhibit jumps as the ray is reflected on boundaries, the ratio $x_\parallel/L$ does not. This ratio is a continuous increasing function varying from 0 to 1 for S_a or from $L_{S_b R_7}/L_b$ to $L_{S_b R_7}/L_b + 1$ for S_b over one cycle.

The local coordinates of P for the first five directed segments of the circuit generated by S_b (A 9*a-e*) are the same as those of the circuit generated by S_a (A 4). As the two sources S_a and S_b go to the critical latitude ($x_{\perp S} \to 0$) from opposite sides, the local coordinates are continuous at the critical lines. In this limit, we also have the following behaviors

$$L_{S_a R_0} \sim \eta, \quad L_{R_7 R_0} \sim \eta, \quad L_{R_4 R_5} \sim 1 - \eta, \quad L_{R_5 R_6} \to 0, \tag{A 12a}$$

$$K_{\perp R_4} \to 0, \quad K_{\perp R_4} K_{\perp R_5} \sim 1/\eta, \tag{A 12b}$$

which guarantee that L_a (A 5) and L_b (A 10) converge towards each other. Thus, the one-cycle distance is also continuous at $x_\perp = 0$ ($\zeta = 0$). The same is also true for the other geometry of $\eta = 1/\sqrt{2}$. This observation makes sure that the asymptotic solution is continuous at the critical lines although the wave beam is split there. This is also justified in the results of the section 3 where no jump is observed at $\zeta = 0$ for the asymptotic velocity profiles.

We then turn to the southward rays in the same geometry ($\eta = 0.35$). These rays propagate along the same circuits as the northward rays but in the opposite direction. Because the geometry and the circuits are symmetric with respect to the diagonal ($r = z$), the southward rays exhibit the same contract/expansion processes on the outer core as the northward rays. The lengths of the directed segments (A 2, A 7) are then unchanged, while the ratios of perpendicular coordinates on the reflection points take the multiplicative

inverse of those of northward rays (A 3, A 8). The one-cycle distances then satisfy the same expressions (A 6, A 11). Finally, similar expressions for the local coordinates as (A 4, A 9) can also be derived.

In the geometry of $\eta = 1/\sqrt{2}$, the relevant expressions for the circuit generated by S_b (light blue line in figure 5*b*) are the same as those in the geometry of $\eta = 0.35$, while those for the circuit generated by S_a (deep blue line in figure 5*b*) are different. However, the two types of circuits in the geometry of $\eta = 1/\sqrt{2}$ actually take the same topology but with different locations of sources. The northward ray generated by the source S_a located at $x_{\perp S}$ can be treated as a southward ray generated by a 'virtual' source S_b' located at the following position

$$x'_{\perp S} = \sqrt{1 - (\eta + x_{\perp S})^2} - \eta. \tag{A 13}$$

The real source S_a is moved backward to the 'virtual' source S_b'. The lengths of the directed segments and ratios of perpendicular coordinates at the reflection points can be obtained using this 'virtual' source S_b'. The same strategy can also be applied to the southward ray generated by the source S_a, where it is treated as a northward ray generated by the same 'virtual' source S_b'. Then the local coordinates and the one-cycle distances can be built using the same approach as before.

REFERENCES

Aldridge, K.D. & Toomre, A. 1969 Axisymmetric inertial oscillations of a fluid in a rotating spherical container. *J. Fluid Mech.* **37** (2), 307–323.

Brouzet, C., Ermanyuk, E.V., Joubaud, S., Sibgatullin, I. & Dauxois, T. 2016 Energy cascade in internal-wave attractors. *EPL (Europhysics Letters)* **113** (4), 44001.

Calkins, M. A., Noir, J., Eldredge, J. D. & Aurnou, J. M. 2010 Axisymmetric simulations of libration-driven fluid dynamics in a spherical shell geometry. *Phys. Fluids* **22** (8), 086602.

Cébron, D., Laguerre, R., Noir, J. & Schaeffer, N. 2019 Precessing spherical shells: Flows, dissipation, dynamo and the lunar core. *Geophys. J. Int.* **219** (Supplement_1), S34–S57.

Cébron, D., Le Bars, M., Noir, J. & Aurnou, J.M. 2012 Libration driven elliptical instability. *Phys. Fluids* **24** (6), 061703.

Dauxois, T., Joubaud, S., Odier, P. & Venaille, A. 2018 Instabilities of internal gravity wave beams. *Annu. Rev. Fluid Mech.* **50**, 131–156.

Favier, B., Barker, A.J., Baruteau, C. & Ogilvie, G.I. 2014 Non-linear evolution of tidally forced inertial waves in rotating fluid bodies. *Mon. Not.R. Astron. Soc.* **439** (1), 845–860.

Favier, B., Grannan, A.M., Le Bars, M. & Aurnou, J.M. 2015 Generation and maintenance of bulk turbulence by libration-driven elliptical instability. *Phys. Fluids* **27** (6), 066601.

Grannan, A.M., Le Bars, M., Cébron, D. & Aurnou, J.M. 2014 Experimental study of global-scale turbulence in a librating ellipsoid. *Phys. Fluids* **26** (12), 126601.

Greenspan, H. P. 1968 The theory of rotating fluids. CUP Archive.

Kerswell, R. R. 1995 On the internal shear layers spawned by the critical regions in oscillatory Ekman boundary layers. *J. Fluid Mech.* **298**, 311–325.

Kistovich, Y. V. & Chashechkin, Y. D. 1994 Reflection of packets of internal waves from a rigid plane in a viscous fluid. *Izv. Atmos. Ocean. Phys* **30**, 752–758.

Koch, S., Harlander, U., Egbers, C. & Hollerbach, R. 2013 Inertial waves in a spherical shell induced by librations of the inner sphere: Experimental and numerical results. *Fluid Dyn. Res.* **45** (3), 035504.

Le Bars, M., Cébron, D. & Le Gal, P. 2015 Flows Driven by Libration, Precession, and Tides. *Annu. Rev. Fluid Mech.* **47** (1), 163–193.

Le Dizès, S. 2015 Wave field and zonal flow of a librating disk. *J. Fluid Mech.* **782**, 178–208.

Le Dizès, S. 2020 Reflection of oscillating internal shear layers: Nonlinear corrections. *J. Fluid Mech.* **899**, A21.

Le Dizès, S. & Le Bars, M. 2017 Internal shear layers from librating objects. *J. Fluid Mech.* **826**, 653–675.

Le Reun, T., Favier, B. & Le Bars, M. 2019 Experimental study of the nonlinear saturation of the elliptical instability: inertial wave turbulence versus geostrophic turbulence. *J. Fluid Mech.* **879**, 296–326.

Lemasquerier, D., Grannan, A. M., Vidal, J., Cébron, D., Favier, B., Bars, M. Le & Aurnou, J. M. 2017 Libration-driven flows in ellipsoidal shells. *J. Geophys. Res. Planets* **122** (9), 1926–1950.

Lin, Y. & Noir, J. 2020 Libration-driven inertial waves and mean zonal flows in spherical shells. *Geophys. Astrophys. Fluid Dyn.* **0** (0), 1–22.

Lin, Y. & Ogilvie, G. I. 2018 Tidal dissipation in rotating fluid bodies: The presence of a magnetic field. *Mon. Not. R. Astron. Soc.* **474** (2), 1644–1656.

Lin, Y. & Ogilvie, G. I. 2021 Resonant tidal responses in rotating fluid bodies: global modes hidden beneath localized wave beams. *arXiv preprint arXiv:2108.08515* .

Maas, L.R.M. 2001 Wave focusing and ensuing mean flow due to symmetry breaking in rotating fluids. *J. Fluid Mech.* **437**, 13–28.

Maas, L., Benielli, D., Sommeria, J. & Lam, F.-P. 1997 Observation of an internal wave attractor in a confined, stably stratified fluid. *Nature* **388** (6642), 557–561.

Manders, A. M. M. & Maas, L. R. M. 2003 Observations of inertial waves in a rectangular basin with one sloping boundary. *J. Fluid Mech.* **493**, 59–88.

McEwan, A.D. 1970 Inertial oscillations in a rotating fluid cylinder. *J. Fluid Mech.* **40** (3), 603–640.

Moore, D. W. & Saffman, P. G. 1969 The structure of free vertical shear layers in a rotating fluid and the motion produced by a slowly rising body. *Phil. Trans. R. Soc. Lond. A* **264** (1156), 597–634.

Morize, C., Le Bars, M., Le Gal, P. & Tilgner, A. 2010 Experimental determination of zonal winds driven by tides. *Phys. Rev. Lett.* **104** (21), 214501.

Mowbray, D. E. & Rarity, B. S. H. 1967 A theoretical and experimental investigation of the phase configuration of internal waves of small amplitude in a density stratified liquid. *J. Fluid Mech.* **28**, 1–16.

Noir, J., Brito, D., Aldridge, K. & Cardin, P. 2001 Experimental evidence of inertial waves in a precessing spheroidal cavity. *Geophys. Res. Lett.* **28** (19), 3785–3788.

Noir, J., Cébron, D., Le Bars, M., Sauret, A. & Aurnou, J.M. 2012 Experimental study of libration-driven zonal flows in non-axisymmetric containers. *Phys. Earth Planet. Inter.* **204**, 1–10.

Noir, J., Hemmerlin, F., Wicht, J., Baca, S.M. & Aurnou, J.M. 2009 An experimental and numerical study of librationally driven flow in planetary cores and subsurface oceans. *Phys. Earth Planet. Inter.* **173** (1-2), 141–152.

Ogilvie, G. I. 2005 Wave attractors and the asymptotic dissipation rate of tidal disturbances. *J. Fluid Mech.* **543**, 19–44.

Ogilvie, G. I. 2009 Tidal dissipation in rotating fluid bodies: A simplified model. *Mon. Not. R. Astron. Soc.* **396** (2), 794–806.

Phillips, O. M. 1966 The Dynamics of the Upper Ocean. Cambridge University Press.

Rieutord, M. 1987 Linear theory of rotating fluids using spherical harmonics part I: Steady flows. *Geophys. Astrophys. Fluid Dyn.* **39** (3), 163–182.

Rieutord, M., Georgeot, B. & Valdettaro, L. 2001 Inertial waves in a rotating spherical shell: Attractors and asymptotic spectrum. *J. Fluid Mech.* **435**, 103–144.

Rieutord, M. & Valdettaro, L. 1997 Inertial waves in a rotating spherical shell. *J. Fluid Mech.* **341**, 77–99.

Rieutord, M. & Valdettaro, L. 2010 Viscous dissipation by tidally forced inertial modes in a rotating spherical shell. *J. Fluid Mech.* **643**, 363–394.

Rieutord, M. & Valdettaro, L. 2018 Axisymmetric inertial modes in a spherical shell at low Ekman numbers. *J. Fluid Mech.* **844**, 597–634.

Rieutord, M., Valdettaro, L. & Georgeot, B. 2002 Analysis of singular inertial modes in a spherical shell: The slender toroidal shell model. *J. Fluid Mech.* **463**, 345–360.

Stewartson, K. 1966 On almost rigid rotations. Part 2. *J. Fluid Mech.* **26** (01), 131.

Thomas, N. H. & Stevenson, T. N. 1972 A similarity solution for viscous internal waves. *J. Fluid Mech.* **54** (3), 495–506.

Thomas, P.C., Tajeddine, R., Tiscareno, M.S., Burns, J.A., Joseph, J., Loredo, T.J., Helfenstein, P. & Porco, C. 2016 Enceladus's measured physical libration requires a global subsurface ocean. *Icarus* **264**, 37–47.

Walton, I. C. 1975a On waves in a thin rotating spherical shell of slightly viscous fluid. *Mathematika* **22** (1), 46–59.

Walton, I. C. 1975b Viscous shear layers in an oscillating rotating fluid. *Proc. R. Soc. Lond. A* **344** (1636), 101–110.